



DIPLOMA THESIS

Microfluidic chip for rapid calcium determination in human milk

Submitted at the Faculty of Electrical Engineering, TU Wien
in partial fulfilment of the requirements for the degree of
Master of Science (Diplomingenieur)

under supervision of

Ao.Univ.Prof. Dipl.-Ing. Dr.techn. Franz Keplinger
Univ.Ass. Dipl.-Ing. Anna Haller

by

Mohammad Amin Managhebaty
Matr.Nr. e1029696
Gschwandnergasse 58/17 - 1170 Wien

April 17, 2017

Statutory Declaration

I declare that I have authored this thesis independently, that I have not used other than the declared sources/resources, and that I have explicitly marked all material which has been quoted either literally or by content from the used sources. Except where otherwise noted, all illustrations are created by author, using free vector graphics editor, Inkscape. Some graphics, however, may contain components from public domain under *CC0*¹ license.

Vienna, _____

¹Creative Commons 0, encompasses all the works, of which the copyright law is waved completely by the creator. Giving attributions are not mandatory upon using the work.

Abstract

Current methods for determination of calcium content in human milk are based on standard laboratory experiments, which are time consuming and require specially trained personnel. Available instruments to accomplish these experiments are usually designed for a sample volume in the range of several milliliters. These approaches are not applicable for in-situ determination of calcium. In this thesis, an inexpensive and rapid technique for quantification of calcium in human milk is presented, using only 5 μ L of sample fluid for operation and determining results within 2-3 minutes. Principles of colorimetric chemical analytical methods are miniaturized to fit a specific microfluidic chip, fabricated based on standard dry film photoresist technology. Downscaling challenges such as fluid flow and mixing, are brought under control after implementation of phaseguides in the chip design and utilizing hydrogel concept, respectively. Future steps can be taken toward developing a compact device to replace the spectrometric instruments, making it an ideal analytical device for non-laboratory environments. This method can also be generalized as a new comprehensive technique for colorimetric assays in micrometer scale for other chemical substances.

Acknowledgments

First and foremost, I would like to take this opportunity to express my deep gratitude to my parents, M.Reza Managhebaty and Zahra Khademian, for their support and love throughout my life.

I would like to express my appreciation to Ao.Univ.Prof. Dr. Franz Keplinger for the opportunity to work in such an interesting field of research. I am especially grateful to Dipl.-Ing. Anna Haller for her support and guidance throughout my work.

Finally, I would like to thank everyone who contributed to the success of this master thesis with their help and support, and all the colleagues at this institute for creating such a friendly environment.

Abbreviations

8HQS	8-Hydroxyquinoline-5-Sulfonic Acid
ASA III	Arsenazo III
BPB	Bromophenol Blue
BSA	Bovine Serum Albumin
CBB	Coomassie Brilliant Blue
CCD	Charge Coupled Device
CPU	Central Processing Unit
DI	Deionized (Water)
EDTA	Ethylenediaminetetraacetic Acid
EM	Electro-magnetic
FAAS	Flame Atomic Absorption Spectroscopy
FWHM	Full Width Half Maximum
GUI	Graphical User Interface
HM	Human Milk
HMA	Human Milk Analyzer
HMB	Human Milk Banks
HMF	Human Milk Fortifier
IQ	Intelligence Quotient
IR	Infra Red
LBWI	Low Birth-weight Infants
LDR	Light Dependent Resistor
LED	Light Emitting Diode
LOC	Lab-on-a-chip
MEMS	Micro Electro-mechanical Systems
MO	Molecular Orbital

MOEMS	Micro Opto-electro-mechanical Systems
NICU	Neonatal Intensive-care Unit
NIR	Near Infra Red
PAA	Poly (Acrylic Acid)
PCB	Printed Circuit Board
PDHM	Pasteurized Donor Human Milk
PE	Polyethylene
PEB	Post Exposure Bake
PEG	Poly(Ethylene Glycol)
PET	Polyester
PMAA	Poly (Methacrylic Acid)
PVA	Poly (vinyl alcohol)
RGB	Red Green Blue
SI	The International System of Units
SMD	Surface Mounted Device
SWIN	Short Wave Infra Red
TAE	Tris-Acetate-EDTA
TBE	Tris-Boric Acid-EDTA
USB	Universal Serial Bus
UV	Ultra Violet
WHO	World Health Organization

Contents

1. Introduction	1
2. Detection, Materials and Methods	3
2.1. Colorimetric Analysis	3
2.1.1. Duboscq Colorimeter Principle	3
2.1.2. Spectroscopy	5
2.1.2.1. Absorption Spectroscopy	6
2.1.2.2. UV/Visible Spectroscopy	9
2.2. Instrumentation and Setup	10
2.2.1. Light Sources	10
2.2.2. Spectrometer	12
2.2.2.1. Monochromator	12
2.2.2.2. Detector	17
2.2.2.3. Optical Resolution	19
2.3. The Beer-Lambert Law	20
2.4. Calcium Detection Method	28
3. Microfluidic Chip for Calcium Detection	30
3.1. Theoretical Background	30
3.1.1. Microfluidic Mixing	31
3.1.2. Filling Micro-channels: Phaseguide Theory	33
3.2. Chip Design	35
3.3. Manufacturing Steps	37
3.3.1. Bottom Slide	37
3.3.2. Top Slide	40
3.3.3. Bonding	44

4. Measurements and Results	46
4.1. Hydrogel Concept	46
4.2. Miniaturized Colorimetric Calcium Determination	50
4.3. Discussion	53
5. Outlook and Conclusion	55
5.1. Compact Colorimetric Analyzer	55
5.1.1. Modifying the Chip	56
5.1.2. The Compact Analyzer	57
5.2. Available Technologies	59
5.3. Conclusion	62
Appendix A. Human Milk Fortifier	63

1. Introduction

Today, there is no doubt that breastfeeding is the best way to feed newborn babies. Several health organizations throughout the world, including World Health Organization (WHO), have suggested exclusive breastfeeding for at least 6 months, starting from the first hour of life [1]. Hundreds of studies from around the world have been conducted over the past decades to compare formula-fed and breast-fed babies. The findings suggest that breast milk provides a better protection against diseases and infections by reinforcing the immune system of the infant. Human milk contains antibodies that are directly related to the pathogens in the mother's environment. Breastfeeding enables babies to receive these antibodies at the early days of life, when the immune system is still too weak to encounter microorganisms [2]. It is also evident that breastfeeding has a positive effect on intelligence quotient (IQ) and educational success [3,4], significantly reduces the rate of neonatal mortality [5,6] and has benefits for mother's health as well [4,6].

Although it is highly recommended, breastfeeding may not be always possible or available for some reasons. Especially for premature and low birth-weight infants (LBWI), it is more likely that mother's milk is not available or does not fulfill baby's nutritional needs. In case of premature birth, babies have to be kept in a neonatal intensive-care unit (NICU) for several weeks and alternative sources of nutrition should be considered: either infant formula or pasteurized donor breast milk. As new studies [7,8] suggest, human milk (HM) from donor mothers should take precedence over artificial formula, since it reduces the incidence of infections and lethal diseases such as severe gut disorder (necrotising enterocolitis) in preterm infants. Growing tendency to use pasteurized donor human milk (PDHM) when mother's own milk is not available, has given a boost to the development of human milk banks (HMB), i.e., a place to collect and process human milk from volunteer mothers to provide nutrition for infants of low birth-weight.

Studies [9–11] on HM have reported a considerable variation in the concentration of macronutrients during the course of lactation, diurnally and between mothers. This fact clarifies the significance of consistent monitoring of the nutritional contents of milk in HMBs, because on the one hand, the digestive system of preterm or low birth-weight

infants can tolerate a limited amount of macronutrient content, but on the other hand, the content of minerals should be of high concentration to cover the infant's need to thrive [12]. In most cases the HM from HMBs (or even mother's own milk) needs to be fortified based on medical prescription to compensate its macronutrient deficits. This requires precise data on nutrient concentration. To perform such monitoring and analysis, fast and reliable detection methods are of significant importance. While conventional biochemical analysis techniques are time consuming, available instruments such as Miris Human Milk Analyzers (Miris Holding AB, Sweden), which are based on mid-infrared detection, cannot detect Ca content.

This thesis presents a rapid analysis method for determination of Ca in human milk based on colorimetric assays on microfluidic chips. First chapter is dedicated to the concept of the colorimetric assays and their application in Ca detection. The aim of this work is to integrate these methods in a single microfluidic chip. This novel branch of science that enables miniaturization of laboratory functions, is referred to as a lab-on-a-chip (LOC). A short presentation on LOCs, as well as the fabrication steps and the necessary background knowledge, is given in second chapter. Results and measurements are presented in the third chapter followed by discussion on possibilities of optimization of the determination technique into a single device in the final chapter.

2. Detection, Materials and Methods

It is necessary to find a practical measurement technique to quantify the amount of substances in a solution. Our work is to evaluate the concentration of micronutrients in human milk based on colorimetric assays. Different concentrations of the sample mixed with a color reagent, results in different shades of the solution. Varying color means different absorption at a certain wavelength. By applying *Beer-Lambert law*, one can link the absorption of light to the concentration of the substance. This method is described in more details in this chapter.

2.1. Colorimetric Analysis

It is regarded as intuitive to expect a darker solution when it contains higher concentration of the substance. This simple color comparison between a series of diluted reference solutions with a known concentration and a solution with unknown concentration has enabled the chemists and biologists since several centuries ago to estimate the amount of substances in the solution. The precise measurement of the unknown concentration was, however, not possible and the procedure was exclusively based on visual comparison. Few attempts were made in the 19th century but among all devices aimed to assign a value to a color, the one invented by a French inventor, Louis Jules Duboscq (1817 – 1886), could be considered as the first practical and easy-to-use colorimeter. Presented in 1854, Duboscq colorimeter has inspired others to modify and further improve the device. Duboscq-based colorimeters were in use until around 1960, when newer technologies have been introduced [13].

2.1.1. Duboscq Colorimeter Principle

Describing the exact colorimeter which was invented by Duboscq is not the aim of this chapter. However, its smart and simple working principle, is a good starting point to understand the colorimetric analysis. As depicted in Figure 2.1, the device consists of

two adjustable glass cylinders (cups) that contain the reference and unknown solutions and two hollow glass tubes with smaller diameters and closed bottom, which are fixed in their positions. The cups can be move in vertical direction by adjusting the screws at the backside of the device, hence, encompassing the glass tubes. Light from the environment

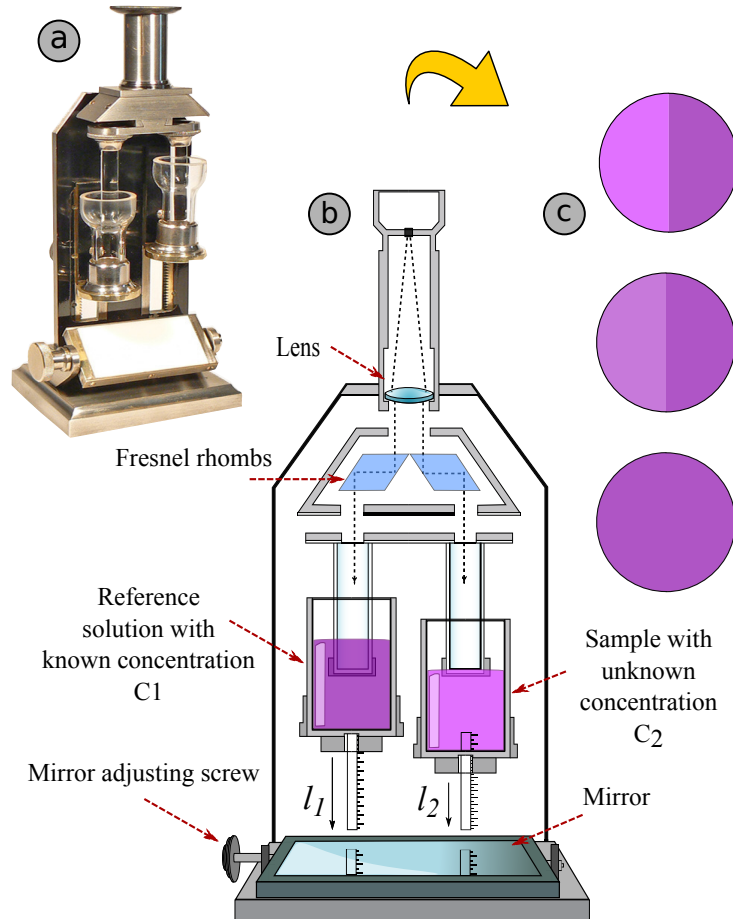


Figure 2.1.: Dubosque Colorimeter a) A Dubosque type colorimeter made by Ph. & F. PELLIN dates back to 1913 [14] b) A mirror underneath the device reflects the ambient light through the cups, that are filled with the reference and unknown solutions, and guides the light to the Fresnel rhombs and the lens. What can be observed from the monocular telescope is two half circles related to each cup c) By adjusting screws at the backside of the device (not shown), heights of the cups, l_1 and l_2 , can be regulated up to the point where the best color-matching is obtained.

is reflected by the mirror underneath, travels upwards, passes the transparent bottom of the cups and reaches the liquids. The lengths of the two paths of light through liquids are crucial parameters in measuring the concentration and can be read off directly from the graduated slits (l_1 and l_2).

The smart characteristic of the Duboscq colorimeter is the use of two *Fresnel rhombs* that guide the light beams to the monocular telescope. While watching through the eyepiece, user observes the standard and the unknown solutions side-by-side in the left- and right-hand side of a circular field. By lowering or raising the cups, one can change the light path through liquids until the desired color-matching is obtained between the two half images. At this point, when the line between the two half-circular images becomes almost invisible, the concentration times the light path for both liquids is equal, that is:

$$l_1 \cdot C_1 = l_2 \cdot C_2 \quad (2.1)$$

Since the concentration of the reference, C_1 , is known, the concentration of the sample, C_2 is the only unknown variable of this equation and can be calculated [13, 15].

Visual comparing of two liquids in terms of their colors lacks precision undoubtedly. Further advancements in this field of science has developed an accurate means of studying color, or more precisely visible light, by introducing the term *absorbance* as the following:

$$A = \log \frac{I_0}{I},$$

where I_0 is the intensity of the incident radiation and I is the intensity of the transmitted radiation through a substance. Conducting an experiment to measure the absorbance value has turned out to be a regular method to quantify color and distinguish between different shades of color, resulted from different concentrations of a substance.

The Beer-Lambert law (explained in Section 2.3), takes one step further and relates the absorption to the concentration and establishes a powerful method to detect and quantify the amount of specific substance in a medium according to its color.

2.1.2. Spectroscopy

Spectroscopy is a general name given to a wide branch of science that investigates the way a matter responses to an electromagnetic (EM) radiation as a function of the wavelength (or frequency). As in quantum theory, EM radiation consists of photons that travel with different frequencies. Energy of each photon is related to its frequency or wavelength as follows [16]

$$E = h\nu = \frac{hc}{\lambda},$$

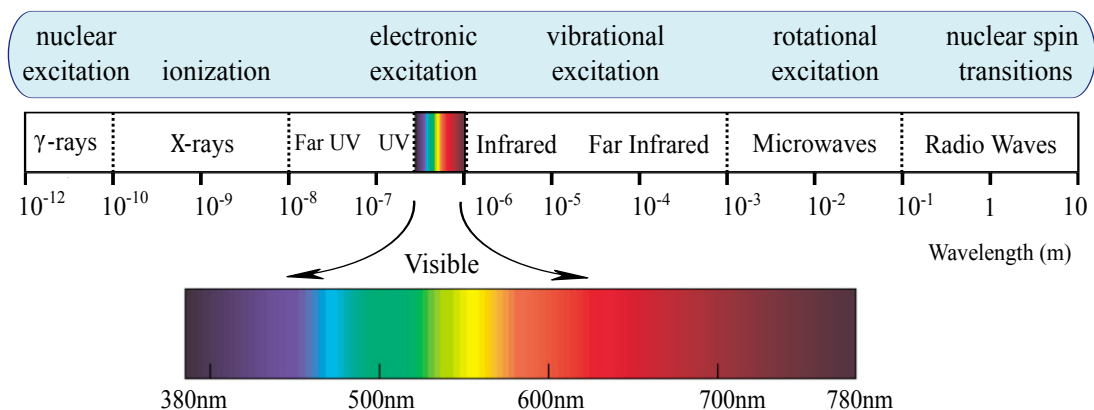


Figure 2.2.: Electromagnetic spectrum and molecular effects associated to each region.

where h is the plank constant ($6.626 \times 10^{-34} \text{ Js}^{-1}$), c is the velocity of light in vacuum ($3 \times 10^8 \text{ ms}^{-1}$), ν is the frequency and λ is the wavelength of the photon. Depending on the wavelength, EM spectrum is divided into several portions; from γ -rays that fall into the range of less than 10 picometers (10^{-11}), up to radio-waves with wavelengths above 1 mm. Each portion of the EM radiation gives rise to specific molecular effect when exposed to molecules or atoms. For example, ultra high frequency X-ray has such a high energy (in the range 100 eV to 100 keV) that can cause an electron to detach completely from the atom; a process that is known as *ionization*. Electromagnetic spectrum, separated in terms of wavelength and the molecular effects related to each region, is illustrated in Figure 2.2. In addition to energy and wavelength, electromagnetic radiations are characterized by velocity, amplitude, phase angle, polarization, and direction of propagation. Spectrometric analysis of a molecule or atom is possible particularly, when the wave-matter interactions lead to a significant (i.e. measurable) change in one or more properties of the radiation.

2.1.2.1. Absorption Spectroscopy

A broad section of spectroscopy analysis deals with the techniques that involves an exchange of energy between the radiation and the matter. A beam of EM radiation strikes a sample under test that probably absorbs particular wavelengths of the radiation. Consequently, the portion of the radiation shows attenuation in specific wavelengths, while other wavelengths remain less affected (Figure 2.3). Absorption of these particular wavelengths has roots in quantum theory, where the energy of the molecules and atoms are

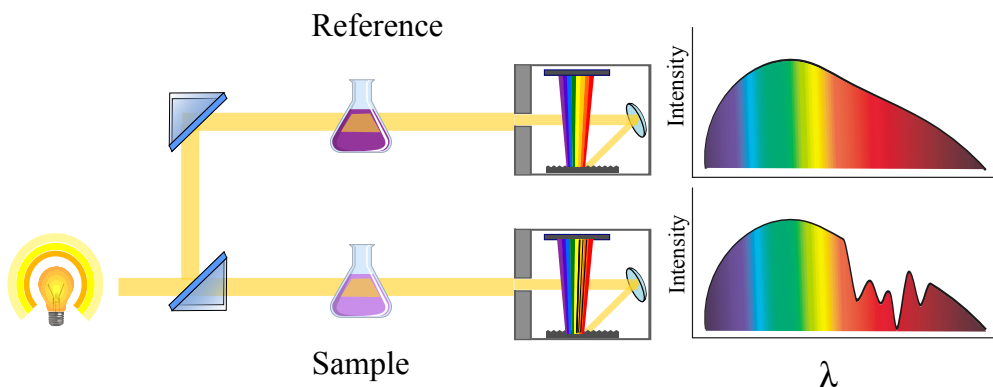


Figure 2.3.: Simplified working principle of a spectrometer. Light passing through the sample shows attenuation in particular wavelengths.

proven to be quantized instead of being continuous as in classic physics. Each molecule or atom has certain discrete energy states. Electrons acquire a certain amount of energy, $\Delta E = E_1 - E_0$, that enable them to excite from the ground state E_0 , i.e., the lowest possible state, to a higher energy state E_1 . This type of transition is called electronic transition. When a beam of radiation passes through a sample, photons carrying the energy ΔE cause the excitation to occur. These photons correspond to a certain wavelength as well (wave-particle duality), that is, their absorption will decrease the energy of the radiation in that specific wavelength. Since the structure of energy states in molecules and atoms is unique, searching for the missed or attenuated wavelengths will help to identify the matter. Electronic transitions occur in the range of ultraviolet and visible radiations [17].

A system in its excited state usually has an extremely short lifetime, tending to go back to the ground state or a lower state and release the excess energy in form of thermal energy or photon emission. The latter gives rise to another widely used technique known as emission spectroscopy. Delayed re-emission of the radiation leads to two other phenomena known as fluorescence and phosphorescence. Other interactions between EM radiations and matter with no energy exchange occur as well, such as diffraction, scattering, refraction or dispersion of radiation. All these modifications of the radiation can be studied as an identification approach [18]. In order not to deviate the aim of this thesis, we focus on *absorption spectroscopy* exclusively.

Vibrational and Rotational Transitions In absorption spectrometry, absorbance, A (Section 2.3) plotted against the wavelength is known as absorbance spectrum. Figure

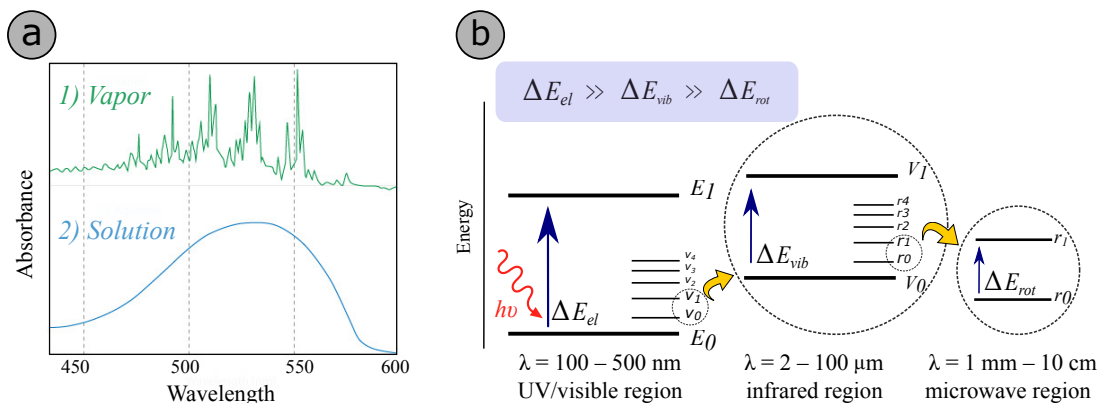


Figure 2.4.: a) Comparison between liquid and vapor phase of a substance b) Electronic energy differences and the wavelength of the absorbed photon. Electronic state consist of several vibrational states and each vibrational state in turn includes rotational energy states.

2.4.a compares the absorption spectrum of a substance in two different phases. The reason for the broad bands of the liquid solution in contrast to the sharp bands of its vapor, lies in the presence of several *vibrational* and *rotational* transitions along each electronic transition in molecules. Atoms are not fixed in a molecule, but rather they show periodic oscillations with very high frequencies, as the atomic bonds undergo stretching or bending. Figure 2.5 demonstrates how atomic vibrational and rotational motions are modeled.

Different modes of vibration and rotation could be assigned to a molecule, each corresponding to a certain energy state [19,20]. Similar to the electronic transitions, transition

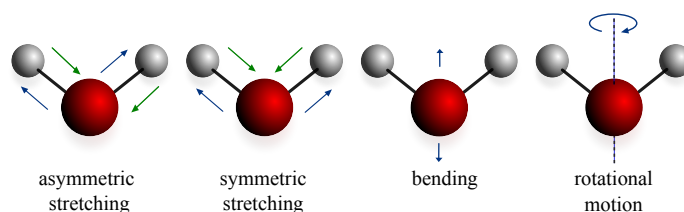


Figure 2.5.: Atoms in a molecular structure are not fixed, but have oscillations around their equilibrium position. Depending on the number of atoms, finite number of geometries exist as a result of these oscillations, which are characterized by a quantum number. Depicted are few models to demonstrate the vibrational and rotational states of a molecule.

from one vibrational or rotational state to another, is only possible when the molecule acquires exactly the amount of energy difference between two states. Each electronic transition in solutions or solids accompanies with several vibrational transitions that need far lower energy to excite. Each vibrational state has in turn many rotational sub-states in several orders of magnitude lower energies (Figure 2.4.b). Consequently, in contrast to the vapor phase that consists merely of the electronic transitions and therefore has sharp peaks in the spectrum, in liquid many other wavelengths are involved that build closely spaced spectral lines, yielding a smoother spectrum ¹. Vibrational and rotational transitions of molecules are studied in Raman spectroscopy as well as in infra-red (IR) spectroscopy [16, 21].

2.1.2.2. UV/Visible Spectroscopy

To gain a better insight into the spectroscopy in ultraviolet and visible regions, a simplified description of the molecular orbital (MO) theory is presented in this Section.

Each atom consists of a certain number of electrons that exist around its nuclei in particular energy levels. When two atoms are brought together, new energy levels (orbitals) emerge, which are different from the initial atomic orbitals in terms of energy. Figure 2.6.a illustrates how two new orbitals appear as hydrogen atoms, ($1s^1$), bind together. The “bonding” molecular orbital, σ , has a lower energy compared to the initial orbitals and the “antibonding” orbital, σ^* , has a higher energy level and is unstable. Similar process merges the p-atomic orbitals to create π -bonding and π^* -antibonding orbitals. In addition, non-bonding orbitals, n , are the orbitals that don’t contribute to the bond order and remain in the same level of energy as the atomic orbital. Depicted in Figure 2.6.b, transitions from MOs could possibly occur when the essential amount of energy is provided by photon absorption. The part of the molecule that absorbs the wavelength in the UV/Visible range is known as *chromophore*. Since the observed wavelength for some transitions falls below the spectral range of measuring instruments, it is favorable to conjugate the chromophores. A conjugated system displays a shift towards higher wavelength (red shift) that makes stronger absorption and hence stronger color [22].

¹The outcome of a measurement is of course dependent on the *optical resolution* of the spectrometer as well (see 2.2.2.3).

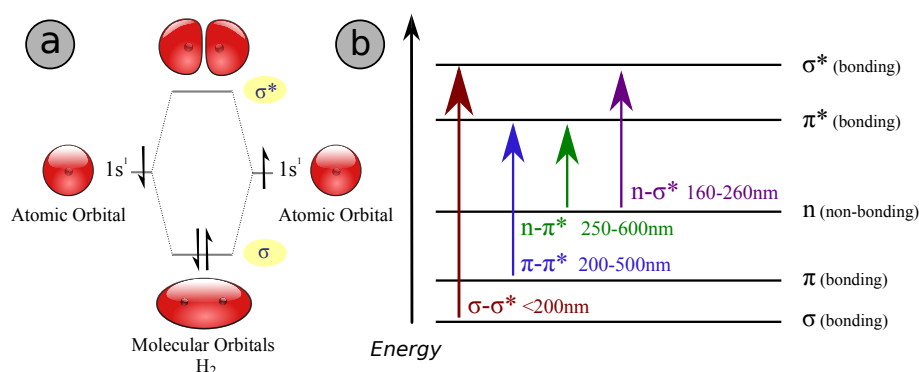


Figure 2.6.: a) Hydrogen has the simplest atomic structure with one electron occupying the first energy level ($1s^1$). After binding together, both electrons fill the emerged σ -bonding orbital and the σ^* -antibonding orbital remains empty. Absorption of light in the UV range causes a transition to the σ^* orbital for a short time b) Possible electronic transitions along with the wavelength required for each.

2.2. Instrumentation and Setup

Figure 2.7 shows a typical setup for a colorimetric analysis of a solution in cuvette. White light is illuminated to a liquid or opaque solid material. Photons with certain wavelength are absorbed by the sample, causing a perceptible attenuation of light in that wavelength. The rest of the light beam is transmitted to a spectrometer that sends the resulted spectral data to a computer for analysis. In this part, a working principle of the utilized measurement instruments will be highlighted.

2.2.1. Light Sources

A source of radiation is the fundamental compartment of the most spectroscopic measurements. Correct choice of light source is the first step toward executing an accurate scientific analysis. Light sources can be divided into two main classes in terms of bandwidth of the produced radiation:

Broadband or continuum sources have radiations in wide range of spectrum and provide a continuous output. Narrowband or line sources, on the other hand, have sharp

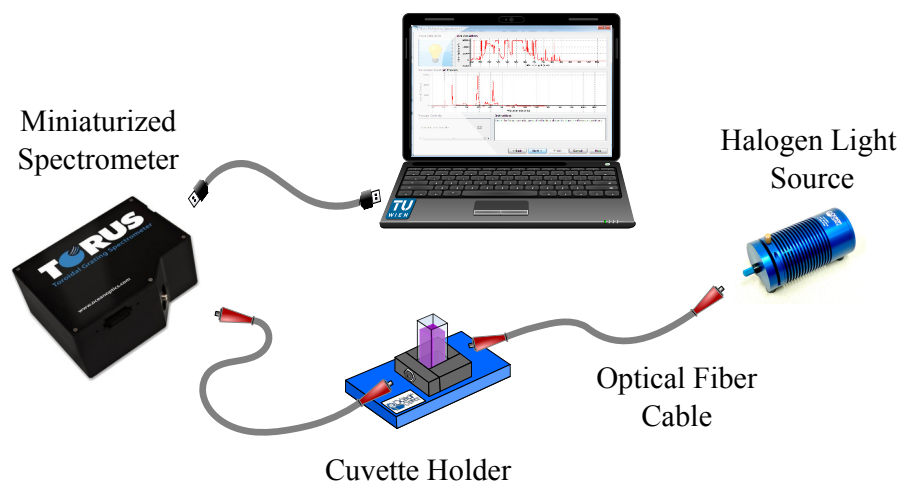


Figure 2.7.: Typical setup for colorimetric measurement consists of a light source, that produces the radiation and directs the light to the sample via fiber cables, a cuvette and its holder, the spectrometer, that receives the light from the sample and converts it to an electrical signal depending on the intensity of light. Data is then sent to a computer for further analysis.

peaks at certain wavelengths. Determined by quantum mechanics, atomic transitions in these light sources can provide an extremely narrow bandwidth of 0.001 nm with a fix position in time, making them the most reliable standards for wavelength calibration in spectrometers [23, 24]. Due to this application, light sources such as mercury-argon (253–1700 nm), neon (540–754 nm), xenon (916–1984 nm), etc. are also known as calibration sources.

The light source used for this work, (HL-2000-FHSA, Ocean Optics, USA), has an integrated tungsten-halogen lamp and provides radiation in the wavelength range from visible to near infrared (NIR), i.e., 360–2400 nm. Comparison between the spectrum of this light source and narrowband mercury vapour light sources is given in Figure 2.8.

As shown in graphs, although tungsten-halogen lamp provides the maximum intensity in the visible range, still most of the radiation energy is dissipated in form of heat with radiations in the infrared region [26]. This is why the lamp housing consists of cooling vents as well as an integrated fan to keep the temperature in the efficient range (usually below 300 °C).

Another feature of a light source is its stability over time, that should be noticed. A light source needs to be warmed up around 10–30 minutes prior to use. Before this time

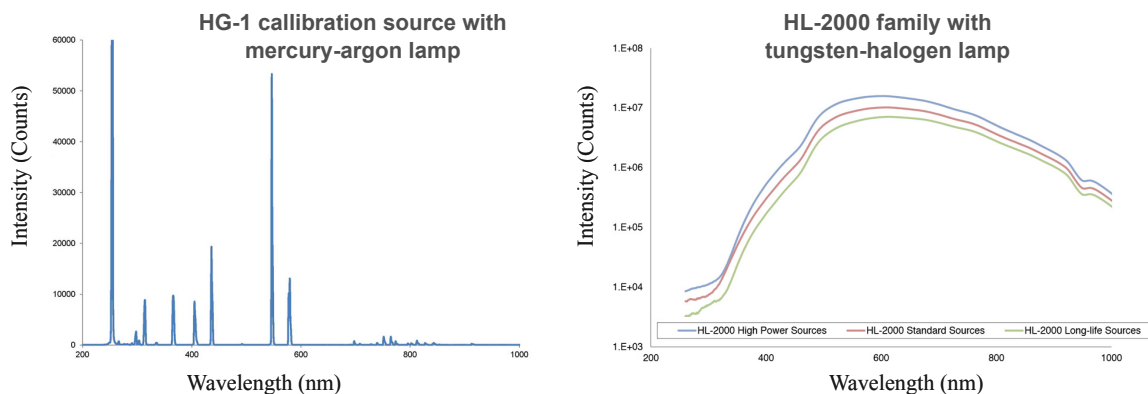


Figure 2.8.: Comparason between the line spectrum of HG-1 mercury-argon calibration source (left) and the continuous spectrum of three products from HL-2000 family with tungsten-halogen lamps (right) [25].

the output shows considerable fluctuations. The graph in Figure 2.9 shows the long-term stability of the output of halogen lamp for different wavelengths. It is important to be aware of such changes while conducting an experiment for obtaining maximum precision. As will be discussed in subsequent sections, absorption measurement is highly dependent on the intensity of the light source. This effect imposes more frequent blanking of the sample, because wide temporal gap between first blank and last measurement could be affected from light source intensity fluctuations and hence error in the results. This data is provided in the user manual of the device. For example, drift of optical output of the light source used in this work, was less than 0.3% per hour.

2.2.2. Spectrometer

Once the light passed through the sample, it is available at the input of the spectrometer. The inherently continuous wavelengths of light should be first separated into finite number of narrow bands, i.e., single wavelength light. This task is performed by a *monochromator*. Afterwards, the intensity of this single wavelength should be registered electronically by means of a *detector*. Finally, the acquired data is sent to a computer [28]. In the following, these two main parts of a spectrometer will be discussed in detail.

2.2.2.1. Monochromator

A monochromator is an optical instrument that extracts a single color from a polychromatic light. Monochromators may utilize glass prism as their dispersive element.

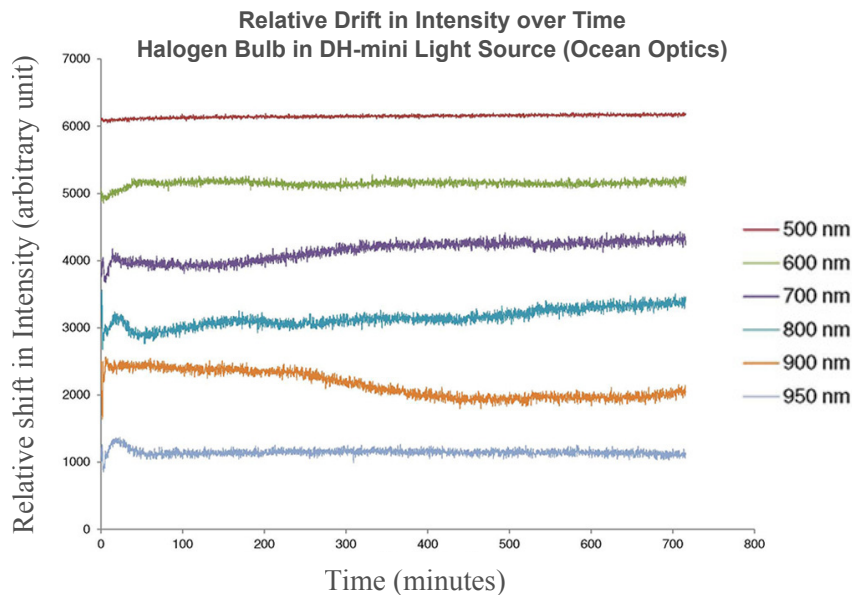


Figure 2.9.: Long-term stability comparison between different wavelengths of halogen lamp for time period of 700 minutes [27].

Dispersion of white light after passing a prism is depicted in Figure 2.10. The incident white light is separated into its constituent monochromatic components as dispersion effect acts differently on each wavelength. To build up a monochromator, a prism and other optical instruments such as mirrors and lenses, are mounted in precisely determined positions, in order to direct the extracted wavelength toward the exit slit. Alternatively, by mechanical rotation of the prism, selecting the desired wavelength at the exit slit is also possible [29].

Most modern spectrometers take advantage of a *diffraction grating*, due to its superior dispersion properties [30] comparing to a prism. Diffraction grating is a dispersive element, consisting of a collection of periodic microscopic grooves, patterned on the surface of a substrate. The density of the grooves per millimeter is a factor indicating the wavelength range of the diffracted light. For instance, gratings used for UV/Vis input light, have densities of several hundreds up to 2000 lines per millimeter.

Two main types of diffraction gratings, *ruled* and *holographic* gratings, have different fabrication processes and optical properties. The master grating of the first type, is fabricated by physically cutting parallel grooves on the aluminium coated surface, by means of diamond tools. The resulted grating has a sawtooth-shaped groove profile. Master holographic gratings, on the other hand, are fabricated on a substrate coated with a photoresist layer. Exposing this layer with two intersecting beams of monochromatic

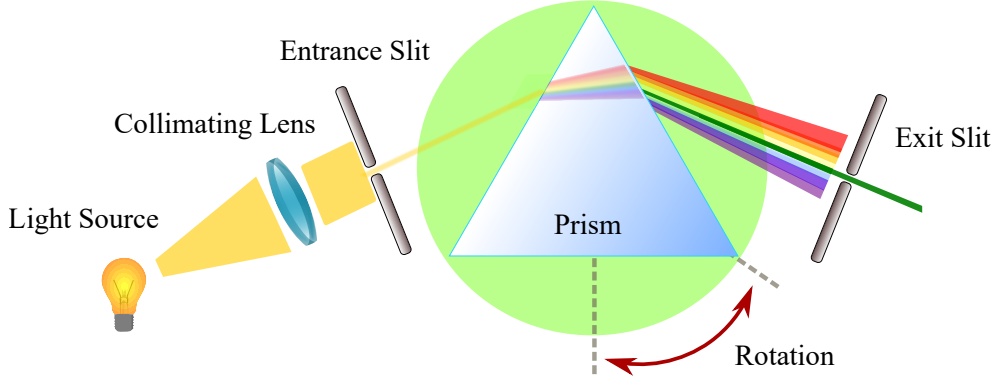


Figure 2.10.: Simplified working principle of a prism monochromator: A narrow beam of white light from the entrance slit passes through the prism and decomposes into its constituent spectrum of colors. By rotating the wheel, on which the prism is fixed, color selection at the exit slit is possible.

light (laser), creates a sinusoidal pattern on the photoresist after developing. Long time of fabrication and extremely high accuracy required for the process, has initially restricted the wide use of these elements. By developing a precision replication process in the late 1940s, replication of hundreds of ruled and holographic gratings from a single master became commercially feasible [31]. A replica of ruled grating, for instance, is structured on a layer of epoxy resin, stuck on a polished glass substrate and coated with aluminium [30].

To gain a better understanding of the dispersion effect, two rays, i_1 and i_2 , of the same wavelength, λ , are supposed to hit a reflection diffraction grating², as in Figure 2.11.a. The beams are incident to the facet of the grating at the angle α . The spacing between adjacent grooves is denoted as d . The diffracted light, β , has by convention a positive sign, when it is on the same side of the grating normal as the incident beam, and negative sign when it is on the other side. As depicted, i_1 and i_2 are in phase at point A and A' . However, i_2 travels a longer path in amount of $C_2 = d \sin \alpha$. There will be a path difference $C_1 = d \sin \beta$, between the diffracted rays r_1 and r_2 as well. The re-emitted waves are in-phase at the points B and B' , if and only if the total geometrical path difference, $C_2 - C_1$, is equal to the integral multiple of the wavelength. This is

² Diffraction gratings are either reflective or transmissive. The latter has a transparent substrate (e.g., glass), that passes through and then disperses the incident light on the other side. The former consists of highly reflective coating on the surface (e.g., aluminium) that reflects the dispersed components of light.

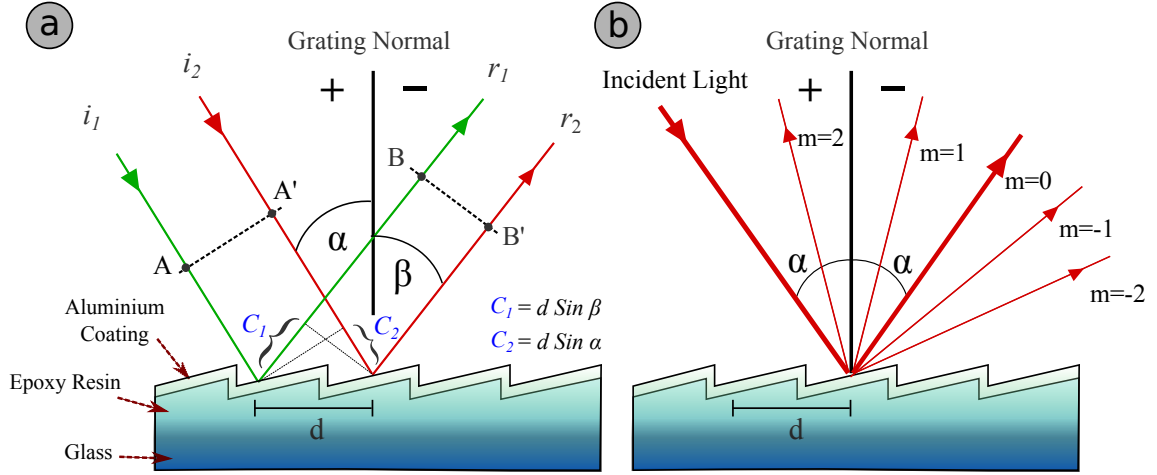


Figure 2.11.: a) Two rays of light, in-phase at the line AA', are also in-phase at BB', if the diffraction equation holds. In-phase waves, undergo constructive interference that results in diffraction of light components with different angle β b) The diffraction equation can be satisfied for different orders m , that is, an incident radiation with wavelength λ , diffracts in multiple directions.

known as the grating equation and is written as follows:

$$m\lambda = d(\sin \alpha + \sin \beta), \quad (2.2)$$

where m is the diffraction order and β has a negative sign. Under this condition, the refracted beams of light undergo *constructive interference*. For a certain wavelength, Equation 2.2 determines all the angles β (depending on the diffraction order m), that are resulted from the constructive interference, whereas waves at all other angles are diminished or completely eliminated due to destructive interference. The stated law is restricted to the configurations where the incident and diffracted light beams are in a plane perpendicular to the grooves.

The diffraction equation can be satisfied by several values of m , known as diffraction orders. Regarding the Equation 2.2, we obtain for m :

$$m \leq |2d/\lambda| \quad (2.3)$$

For example, for a diffraction grating with 1666 lines/mm, d is equal to 600 nm. The incident monochromatic light beam with wavelength $\lambda = d$ results in 5 values for m : -2,

-1, 0, 1 and 2. The zero order ($m = 0$), is always available and occurs when the incident and emitted light beams have the same angle with respect to the grating normal, i.e., $\alpha = -\beta$ for all values of λ . This is known as specular reflection. Complete mirror behaviour of a grating happens when the groove distance d is smaller than $\lambda/2$ and the only integer that satisfies Equation 2.3 is $m = 0$. By convention, sign of the diffraction orders are determined in respect to the zero order (Figure 2.11.b) [30,32–34].

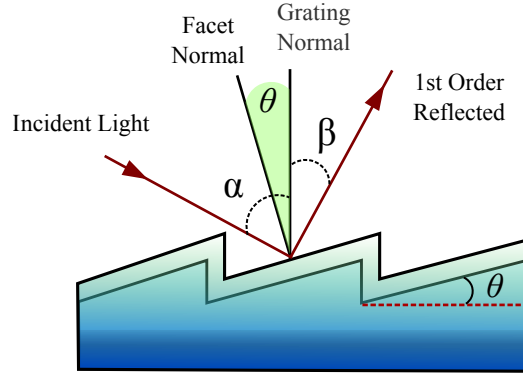


Figure 2.12.: Blaze condition can be obtained by tuning the sawtooth angle of the grooves θ and adjusting the angles of the incident and the diffracted beams, α and β , in a manner that the diffracted beam corresponds to specular reflection off the groove facet.

Blaze Condition The amount of energy distributed in higher diffraction orders, reduces the light utilization efficiency. For most monochromators, gratings are designed in a manner to consist only the 1st order. However, the efficiency of the diffracted light within the order, is not uniform for all wavelengths. The wavelength of incident light that results in highest efficiency, is referred to as the *blazed wavelength*, λ_b . This wavelength is usually provided in the spectrometer's specifications. Approximately, the signal strength for a blazed ruled grating, undergoes 50% drop at $0.6 \lambda_b$ and $1.8 \lambda_b$. In ruled diffraction gratings, the blaze condition is tuned by the *blaze angle* θ , i.e., the angle of the sawtooth shape grooves relative to the substrate. This angle geometrically equals the angle between the grating normal and the facet normal of each groove (Figure 2.12). Maximum efficiency of the selected order is achieved, if the blaze condition is satisfied, that is when the facet normal bisects the incident and diffracted beams. In this case, the facet of the groove acts as a tiny mirror, therefore:

$$\theta = (\alpha + \beta) / 2, \quad (2.4)$$

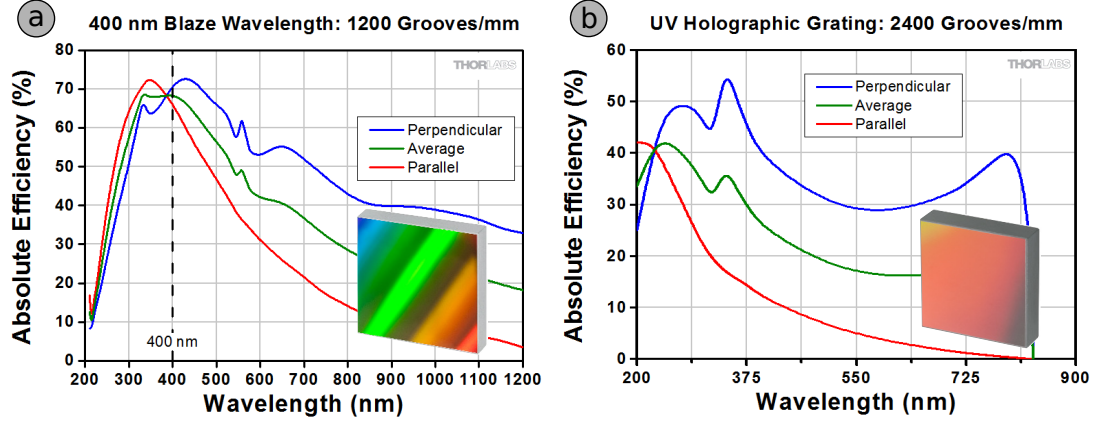


Figure 2.13.: Efficiency curves of a) ruled and b) holographic diffraction gratings are compared for parallel and perpendicular polarizations. While the former shows a peak around the blaze wavelength of 400 nm, the latter is more flat within the wavelength range [37].

where, α and β are the angles between incident and diffracted light to the grating normal, respectively. As stated for the grating equation, sign of β is taken as positive if the reflected light is on the other side of the grating normal with respect to the incident light. This equation, together with Equation 2.2, can be used to indicate the values of α and β of the configuration, to blaze at a particular wavelength. [32,35,36].

Holographic gratings have generally sinusoidal profile. Although providing less light scattering comparing to ruled gratings, they exhibit comparatively lower but flat efficiency curves. Blazed holographic gratings can bring the advantage of higher efficiency around specific wavelength. Different blazing techniques for holographic diffraction gratings are compared by M.Breidne et al. [38].

Efficiency curves of ruled and holographic gratings are compared in Figure 2.13. Absolute efficiency is defined as the ratio of the output energy to the input energy at each wavelength [35].

2.2.2.2. Detector

The detector is the last element to which the light beam enters. A simple spectrometer can be brought together by placing a photo diode at the exit slit in Figure 2.10. The intensity of the monochromatic light, incident on the detector, is converted to electrical signal. Rotating the prism enables the detector to register intensity values of different wavelengths within the scanned interval, which is then transferred to a computer for fur-

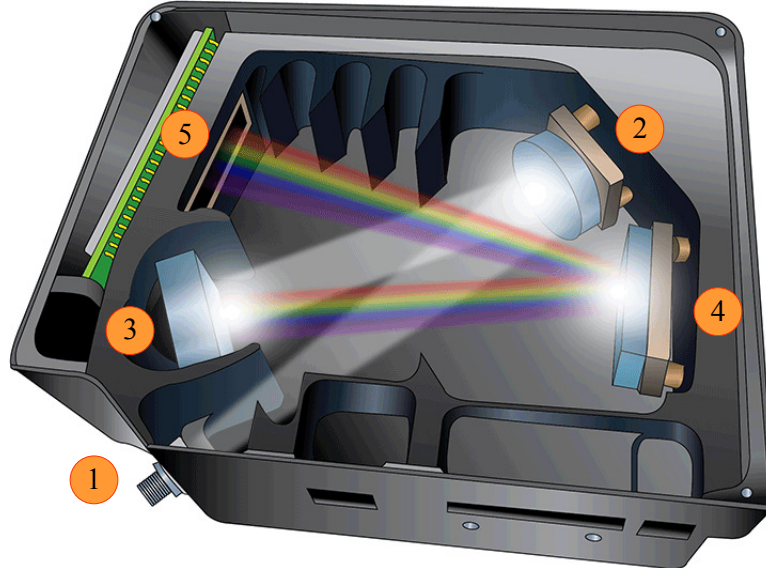


Figure 2.14.: Optical configuration of a spectrometer consists of 1) fiber connector or alternatively entrance slit with selective width, 2) collimating mirror, 3) diffraction grating, 4) focusing mirror and 5) detector array [39].

ther analysis. In advanced spectrometers with a substituted diffraction grating, however, rotation compartments and the exit slit are eliminated by introducing a linear detector array. This simplification has led to considerable reduction of the cost and size of the spectrometers. Figure 2.14 depicts the optical configuration of a commercially available miniaturized spectrometer (Maya2000 Pro, Ocean Optics, USA). In this configuration, the light is guided into the spectrometer via an optical fiber cable. Spectrometers usually provide an additional user-selectable slit with several aperture width to cover different applications. The input light from the optical fiber needs to be collimated by means of a precisely positioned collimating mirror. Need for collimated light is comprehensible according to Equation 2.2. Ideally, for collimated beams of light, the angle of incidence α , is equal at each groove surface. Hence, a unique diffraction angle β , is obtained from the equation for each wavelength. Without the collimating mirror, the divergent beam will hit the surface of the grating with different angles and several β s for each wavelength will be resulted. The detector will then register several pixels for a particular wavelength, which is not acceptable [40]. After diffraction, a focusing mirror forms the dispersed wavelengths of the first order on the linear detector array. Alternatively, utilizing concave holographic gratings can eliminate both mirrors from the configuration, leading to higher efficiency and smaller devices [41].

The detector array in miniaturized spectrometers is frequently fabricated from silicon

or InGaAs alloy. These materials apply a limit to the maximum detectable wavelength of the detector. Maximum detectable wavelength for InGaAs detectors, can be tuned by changing the alloy composition to cover the near infrared (NIR) and short wave infrared (SWIR) regions from $0.8\text{ }\mu\text{m}$ to $2.5\text{ }\mu\text{m}$ [42, 43].

Silicon, on the other hand, is the main material to fabricate a charge coupled device

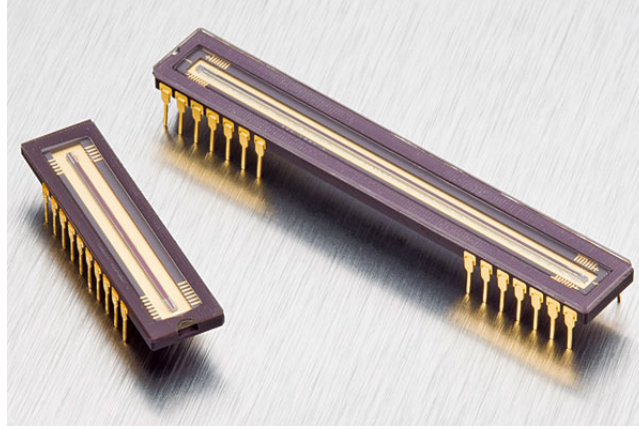


Figure 2.15.: Excelitas CCD linear sensors are available in array lengths of 512-, 1024-, 2048-, and 4096 pixels and provide a line scan rate of 70 kHz [44].

(CCD) light sensor with maximum detectable wavelength of about 1100 nm . A linear³ CCD light sensor (Figure 2.15) is an array of photosensitive elements (pixels). Upon exposure to radiation, electron charge is created in each pixel relative to the intensity of the perceived light. The accumulated charge of each pixel is then transferred sequentially in one direction along the array, enabling the read-out to be accomplished from the last pixel of the array⁴. Charge transfer rates as high as tens of kilohertz with negligible data loss, high efficiency and low noise, has turned CCD sensors to an ideal choice in many light detection applications [45, 46].

2.2.2.3. Optical Resolution

Optical (or spectral) resolution of a spectrometer is an important characteristic of the device, indicating the ability of the device to separate adjacent spectral peaks. What we assumed so far as a single wavelength light (monochromatic), is in reality a narrow band of wavelengths. For example, bandwidth of a monochromatic light at 600 nm ,

³Two dimensional CCD sensors find wide application in imaging devices and cameras.

⁴Read-out circuit can be integrated at both ends of the sensor, leading to higher data transfer rates.

expressed as the full width at half maximum (FWHM), extends from 599.5 to 600.5 nm. The optical resolution of such system is said to be 1 nm, that is, within the range 300 to 800 nm for visible light spectroscopy, maximum number of 500 points (wavelength peaks) will be resolved.

Considering the optical configuration in Figure 2.14, the optical resolution can be affected by three elements: the slit width, groove density of the diffraction grating and the detector.

Reducing the entrance slit width will increase the resolution, but, on the other hand, the intensity of the radiation decreases. The higher the groove density, the more orders of diffraction appear. This increases the dispersion but reduces the spectral range accordingly. Ultimately, the number of detector elements (pixels) determines the number of wavelength peaks that can be digitized.

Although provided by the manufacturer, optical resolution can be approximately calculated to better reveal the dependencies to the mentioned factors. For a particular spectrometer, dispersion (nm/pixel), is given by dividing the spectral range of the grating by the number of the detector pixels. Calculated dispersion multiplied by the pixel resolution results in the optical resolution. Pixel resolution, is the average number of pixels, dedicated to resolve each wavelength band. Depending on the slit width, the number of illuminated pixels can differ from about two pixels for narrow slits up to several tens of pixels for wide slits and fiber optic cables. This data is usually provided in the device specifications from the manufacturer [30, 35, 46, 47].

2.3. The Beer-Lambert Law

So far, we learned how the curve of absorption versus wavelength (absorbance spectrum) of a sample (solution, gas etc.) is obtained from spectrometer. Next step is to use the absorption to calculate the concentration of the molecules or atoms in the solution. Spectrometers usually calculate the absorbance from transmittance. Assuming a monochromatic radiation illuminated to a sample, the transmittance, T , is defined as [48, 49]:

$$T = I_{\lambda}/I_{0,\lambda}, \quad (2.5)$$

where I_{λ} ⁵ and $I_{0,\lambda}$ are the *irradiance* of the transmitted light and the incident light at wavelength λ respectively. Irradiance is the radiant power per unit area (W/m²).

⁵The subscript notation λ will not be used from now on due to the monochromatic light assumption.

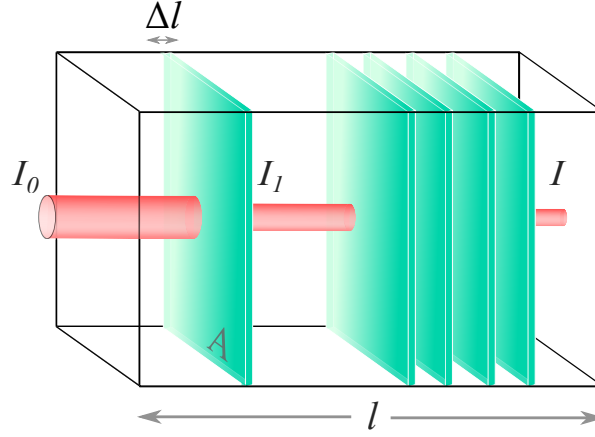


Figure 2.16.: The sample is divided into N segments with the width Δl and area A . Intensity of the input radiation, I_0 , reduces to I_1 when passing the first segment.

Transmittance has no unit and is usually given as percent. To simplify our calculations, we neglect the reflected and scattered portion of the light. Transmittance below 1 (100%) means the sample has absorbed a portion of the input power. To find out the Beer-Lambert law, we need to take a closer look at the optical absorption phenomena.

First we assume an isolated molecule that is exposed to a monochromatic illumination. The amount of power absorbed is proportional to the irradiance (also called intensity) and can be written as:

$$W = \sigma \cdot I_0 \quad (2.6)$$

Since W is in watt, the proportionality factor, σ , indicates an area (m^2). This area is defined as the effective photon-capturing area, engaged with the probability of the absorption of energy. Not all photons colliding with a molecule can be absorbed; therefore, the *absorption cross-section*, σ , is much smaller than the geometrical cross-section of the particle [50]. Absorption cross-section is depending on the wavelength of the incident light [51].

Next, we expand our initial assumption from a single molecule to a homogeneous sample (e.g. liquid sample) that contains M molecules per unit volume (cm^{-3}). As depicted in Figure 2.16, the sample is divided into N segments with area A and thickness Δl [48, 52]:

$$l = N \cdot \Delta l \quad (2.7)$$

Molecules are assumed to be located in a distance apart from each other in a way that the inter-molecular interactions are negligible. The number of molecules in each seg-

ment counts $MA\Delta l$ and the total cross section for all molecules inside the segment is $\sigma_t = \sigma MA\Delta l$, where σ is the cross-section of a single molecule as stated before.

When the beam with irradiance I_0 enters the first segment (Figure 2.16), W/A of the radiation power per unit area is absorbed. Total amount of absorbed power is obtained when σ in Equation 2.6 for a single molecule, is replaced by σ_t for M molecules. Therefore:

$$\begin{aligned} I_1 &= I_0 - \frac{W}{A} = I_0 - \frac{\sigma_t I_0}{A} = I_0 \left(1 - \frac{\sigma_t}{A}\right) \\ I_1 &= I_0 \left(1 - \frac{\sigma MA\Delta l}{A}\right) \\ \Rightarrow I_1 &= I_0 (1 - \sigma M\Delta l) , \end{aligned} \quad (2.8)$$

where I_1 is the irradiance leaving the segment number one. The same calculation gives the I_2 :

$$I_2 = I_1 (1 - \sigma M\Delta l) = I_0 (1 - \sigma M\Delta l)^2$$

Consequently, I , the irradiance leaving the sample (N_{th} segment) can be written in terms of I_0 as following:

$$I = I_0 (1 - \sigma M\Delta l)^N , \quad (2.9)$$

where $\Delta l = l/N$ (Equation 2.7). Substituting $-(\sigma Ml)/N$ with $1/k$ we have:

$$I = I_0 \left[\left(1 + \frac{1}{k}\right)^k \right]^{-\sigma Ml} \quad (2.10)$$

When the number of segments, N , becomes indefinitely large ($N \rightarrow \infty$ and hence $k \rightarrow \infty$), the expression given in brackets in the Equation 2.10, turns out to be the limit that defines the exponential function:

$$\lim_{k \rightarrow \infty} \left(1 + \frac{x}{k}\right)^k = e^x$$

Equation 2.10 can therefore be written as [53]:

$$\frac{I}{I_0} = \exp(-\sigma Ml) \quad (2.11)$$

This is called the law of exponential attenuation by absorption [50] and was first mentioned by the French mathematician, Pierre Bouguer, in 1729. He found a relationship between the reduction of the radiation power and the thickness of the sample i.e. the pathway of light through the sample.

By taking the *log* of both sides of the Equation 2.11 we reach a definition for the absorbance, A , (without unit) of the sample under test:

$$A = -\log\left(\frac{I}{I_0}\right) = \sigma M l \log e$$

Since M is the number of molecules in unit volume, it can be substituted with $N_A \cdot C$, where N_A is the *Avogadro* constant (6.02214×10^{23} (mol⁻¹)) and C (mol cm⁻³) is the concentration of the solute:

$$\sigma M l \log e = \sigma N_A l C \log e = \varepsilon l C$$

Molar absorptivity, or extinction coefficient, ε , has the unit (cm² mol⁻¹) or (M⁻¹ cm⁻¹) in the international system of units (SI).

Finally, the Beer-Lambert law can be derived as a linear equation that links the absorption with the thickness and concentration of the solution:

$$A = \varepsilon l C \quad (2.12)$$

This is the equation used by Duboscq (Section 2.1.1) in his colorimeter. Both tubes have the same absorption after adjustment due to identical color and since the substances are chosen to be the same as well, ε , also remains constant. Hence, the relationship $C_1 \cdot l_1 = C_2 \cdot l_2$ appears, in which the only unknown variable is the concentration C_2 of the sample under test.

From Equation 2.5, a relationship between absorbance and transmittance can be derived:

$$A = -\log\left(\frac{I}{I_0}\right) = -\log T \quad (2.13)$$

It is evident, that the thickness and/or concentration have no linear connection with transmittance.

Calibration of the Spectrometer To obtain the amount of absorption from a spectrometer according to Equation 2.13, a liquid sample in an optically clear container, for example a cuvette, is exposed to a beam of light from one side and a photo detector collects the illuminated light from the other side of the container. In order to reach the Beer-Lambert law in the previous section, we simplified the procedure by neglecting the scattering and reflecting, and assumed that all the unabsorbed photons reach the photo detector sensor. This is however far from reality and can cause considerable error. To solve this issue calibration of the device should be considered prior to use. Calibration

will minimize the impact of the environmental parameters, such as the ambient light that reaches the detector without passing the sample (stray lights), as well as unwanted absorption by the container itself and impurities in the sample's matrix. This is done by setting a reference point that is chosen to have zero absorption and proceeding the measurement with respect to this point. The reference (also called *blank*) contains zero concentration of the substance under test in the exact same solution (color reagent, buffer etc.) as the sample solution. The following calculations shows how the blank spectrum is extracted from the sought data. As depicted in Figure 2.17, A_b and A_s are the absorptions of the blank and the sample, respectively:

$$A_b = -\log(I_b/I_0)$$

$$A_s = -\log(I_s/I_0)$$

Rewriting (I_s/I_0) as $(I_s/I_b)(I_b/I_0)$, we get:

$$\begin{aligned} A_s &= -\left(\log\left(\frac{I_s}{I_b}\right) + \log\left(\frac{I_b}{I_0}\right)\right) = -\log\left(\frac{I_s}{I_b}\right) + A_b \\ \Rightarrow A_s - A_b &= -\log\left(\frac{I_s}{I_b}\right) \end{aligned} \quad (2.14)$$

A_b in Equation 2.14 is set to zero by device and the absorption of the sample is obtained from the spectrometer, as the ratio of the output intensity of the sample to that of the blank. Once the value of I_b is provided, it is stored in the spectrometer for further calculations of the absorption of the sample in different concentrations.

As an electronic device, the photo detector itself shows contributions of noise from different sources. This effect is taken into account by turning off the shutter of the light

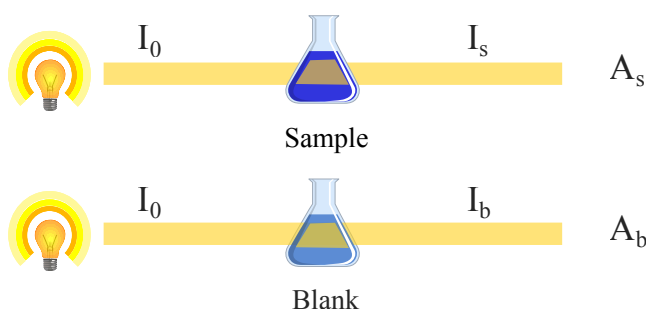


Figure 2.17.: To eliminate the effect of absorption by other substances than the one under test, “blanking” should be considered as well.

source for few seconds. With no input light, the detector still registers the *dark* intensity as a result of noise, which is subtracted according to the following relation [54, 55]:

$$A_s = -\log\left(\frac{I_s - I_d}{I_b - I_d}\right), \quad (2.15)$$

where, A_s is the absorbance of the sample, I_s is the intensity of the light that passes the sample and reaches the photo diode, I_b is the intensity of the light that passes the blank and reaches the photo diode, and I_d is the dark intensity ⁶.

Limitations of the Beer-Lambert Law The Beer-Lambert law, Equation 2.12, shows a linear relationship between absorption of light and concentration of analyte in the sample. This is however not always the case; in practice, the A-C curve (standard or calibration curve) shows deviations from the law specially at higher concentrations. The reason lies in the initial assumptions we made to reach the Beer-Lambert law. First, as mentioned in the Section 2.3, molecules were considered to be isolated and the possible intermolecular interactions were neglected. This assumption does not hold for higher concentrations where reduction of the absorption cross-section of the molecules due to overlapping and shading effects are expected. On the other hand, a monochromatic wavelength is necessary for linearity of the Beer-Lambert law. In reality, the measurement devices provide an approximate narrow band of wavelengths instead. Wavelength dependence of the molar absorptivity, ϵ , may cause non-linear behaviour of the curve [21, 56, 57]. This error can be minimized to obtain a more reliable linear curve, by means of spectrometers with higher *optical resolutions* (Section 2.2.2.3). Regarding the higher cost of the spectrometric instruments with better resolution, the analyst faces a trade-off between the required precision of the results and the available budget. Apart from that, for preparing the standard curve, which is the first aim of most determination measurements, the wavelength of maximum absorbance, λ_{max} , should be taken into account (Figure 2.18). The wavelength bandwidth is determined by the optical resolution of the device and is assumed equal for both measurements at points A and B. Comparing the gradients at these two points reveals the least variations of absorption value for the point A, with lowest slope (ideally zero). In a similar manner, point B encompasses huge fluctuations in absorbance within its same bandwidth, that results in a non-linear

⁶This relationship is acquired for *single-beam* spectrophotometers. In *dual-beam* spectrophotometers, however, a continuous comparison of the sample with the reference is made as a result of two beams of light passing through them simultaneously

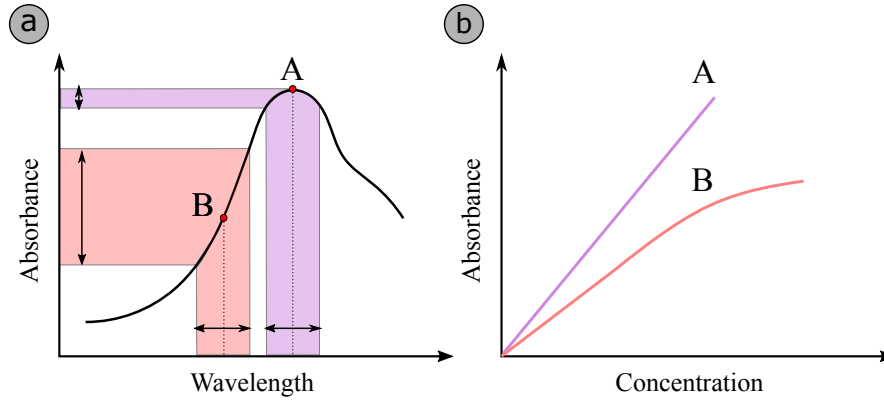


Figure 2.18.: a) Restricted by the optical resolution of the spectrometer, two wavelength bands of identical width are assumed to estimate the absorbance at points A and B. The absorbance in point A (λ_{max}), has less variations in comparison to point B, due to higher gradient of the curve at this point b) standard curve, obtained based on the wavelength of the maximum absorbance, behaves more linearly and is more reliable.

standard curve. [49].

Standard curve preparation In routine laboratory tasks, there are handbooks and references available that contain all required amounts of extinction coefficients, ε , at certain wavelengths. In order to find the concentration of a substance, the analyst needs to find the absorbance from the spectrometer and calculate the concentration from the Beer-Lambert law. Such references do not always exist. Another method is to prepare a series of solutions with exact known concentration of the substance and find the absorbance for each at the highest absorption wavelength, λ_{max} . Then find the best-fit line in the plot absorbance against concentration. This is the so-called *standard curve* (or calibration curve). By having the standard curve available, unknown concentration of the solution can be read from it, according to the absorbance extracted from the spectrometer at the same wavelength [58].

The slope of standard curve is the extinction coefficients, ε , and is expected to be a line passing the origin. As discussed in the previous section, this is not always true, specially at higher concentrations the curve tends to become saturated, i.e., higher concentrations of the substance do not contribute to higher absorbance any more. For reliable evaluations, it is important to work in the linear range of the standard curve.

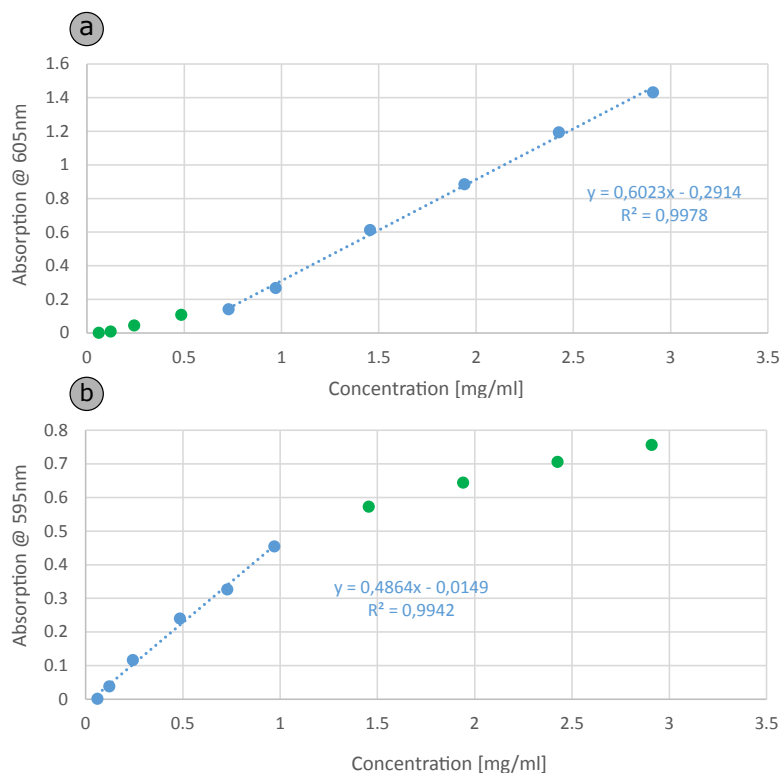


Figure 2.19.: Standard curves of BSA determination from two different assays a) bromophenol blue is used as the stain reagent and the absorption peak at 605 nm is considered. The linear behavior of the graph achieved for concentrations above 0.5 mg/ml of BSA b) Bradford assay uses coomassie brilliant blue dye and the absorption peak appears at 595 nm. linearity of the measurement points is best for concentrations below 1 mg/ml of BSA.

In case that the obtained absorbance extends beyond linear region, stepwise dilution of the sample solution, should be considered. After returning back to the linear range, the dilution ratio must be taken into account in the final estimations. This is how the *upper boundary* is defined. The *lower boundary* depends on the accuracy of the measurement instruments. Very low amount of absorbance of very diluted samples can be off-scale, resulted from noise and/or device failures. Figure 2.19 shows calibration curves of two colorimetric assays for determination of bovine serum albumin (BSA) protein. Figure 2.19.a relates to the assay, that uses bromophenol blue (BPB) as a staining reagent. Absorption spectrum of the BPB shows two peaks at 435 nm and 591 nm. Upon interaction with BSA, the resulted mixture undergoes a significant increase and shift of the absorp-

tion peak from 591 nm to 605 nm [59]. This wavelength is of interest for investigating the absorption change in accordance with BSA concentration. The obtained standard curve is linear for concentrations above 0.5 mg/ml. Another assay is introduced by M. Bradford [60], that uses coomassie brilliant blue (CBB) to stain the BSA solution. This binding causes a shift of maximum absorption from 465 nm to 595 nm. The standard curve for this assay, Figure 2.19.b, behaves linearly for concentrations up to 1 mg/ml.

In both mentioned graphs, the linearity of the set of points is estimated by simple linear regression using a software. The aim of this approach is to construct a *trendline*, also referred to as the line of best fit, in form of $y = ax + b$, that best describes the general pattern of a set of data. Along with the line, the coefficient of determination (R^2), is also provided by the software, indicating how good the estimation is fulfilled. R^2 can take values between 0 and 1. In the ideal case, where the trendline passes all the data points, R^2 is equal to 1. The standard curves of BSA assay have R^2 values very close to 1, indicating a good linear behaviour of the curve.

Next Section is dedicated to the colorimetric detection of calcium in a cuvette, to clarify all the discussed topics so far, as well as to give a better insight into the detection procedure performed with slight changes to fit the microfluidic chip.

2.4. Calcium Detection Method

The metallochromic dye arsenazo III (*ASA III*) has long been in use as a sensitive calcium ion (Ca^{2+}) indicator. Arsenazo III is available in powder form, and its solution exhibits a maximum absorption at around 540 nm at pH 7.4. Its spectra however undergoes spectral changes upon complexation with cation Ca^{2+} , that is, the absorption peak shifts to around 610 nm and a new peak appears around 655 nm at the same pH value [61]. Chemical formula of ASA III and its absorption spectrum with and without binding Ca^{2+} ions is depicted in Figure 2.20. Despite its high binding constant for Ca^{2+} ions comparing with other dyes [63], ASA III has several drawbacks that need to be considered in the colorimetric assays. First thing to mention is the strong pH dependency of the dye upon its interaction with metal ions. With a constant amount of Ca^{2+} ions, absorption value of the complex increases linearly by transition from acidic to alkaline medium and reaches its maximum at the pH around 9 [64,65]. Conducting the assay in alkaline medium however gives rise to another drawback of the ASA III dye; its interference with magnesium ions (Mg^{2+}). This is due to the fact that calcium binding to the ASA III is competitively inhibited by Mg^{2+} ions, that causes spectral changes similar

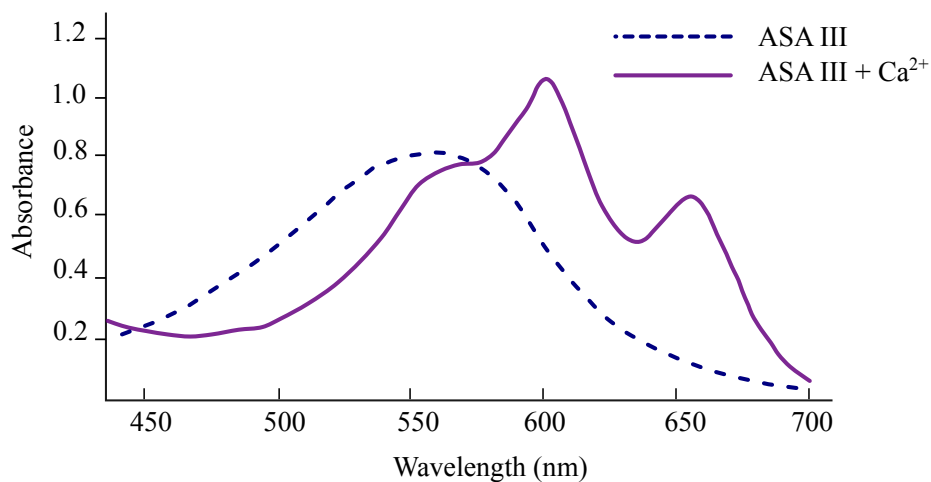


Figure 2.20.: Recreated graph from [62] shows the absorption spectrum of ASA III in the presence and absence of calcium ions.

to the Ca^{2+} case and, therefore, uncertain estimation of the calcium content [66]. This effect is negligible in acidic environment, however, higher values of absorption can be obtained in basic reagents, if this interference can be handled in a proper manner. Suggested by B.R.Morgan et al. [65], Mg^{2+} content of the sample can be masked effectively by including 8-hydroxyquinoline-5-sulfonic acid (*8HQS*) to the reagent.

Finally, running these colorimetric experiments requires high level of caution due to toxicity of the arsenazo III reagents.

3. Microfluidic Chip for Calcium Detection

Microfluidics can be regarded as a subset of MEMS (*Microelectromechanical systems*), that has been developed to handle and control flow of liquids in micro channels. Taking advantage of silicon (Si) microelectronics and relevant fabrication techniques at the early stages, microfluidics soon found its own methods and materials to fulfil the requirements of specific applications in chemical and biological analysis. In this regard, silicon and associated technologies have been largely replaced by plastics and polymers; a trend that led to development of a new fabrication methods which are low-cost and fast. Beside the ease of fabrication, microfluidic devices enable the scientists to carry out experiments with sample quantities as small as several microliters or less, which drastically reduces the cost of analysis as well as the risk of working with harmful materials and infectious agents. Recent advancements in microfluidics has given rise to the lab-on-a-chip (LOC) concept, i.e., the idea to integrate all the applications required for a thorough analysis into a single chip. Much research has been devoted to investigate new aspects of the lab-on-a-chip concept, nevertheless it doesn't meet the commercialization factors in many fields yet [67,68].

In this thesis, a LOC device on a glass substrate is presented to detect and quantify the amount of calcium in human milk. The colorimetric assay, introduced in previous chapter, is miniaturized into a microfluidic chip. In this Chapter, we first take a look at the theory of micro-scale flow and then demonstrate the fabrication steps of our chip. Next Chapter will be dedicated to the measurements on the chip.

3.1. Theoretical Background

The basics of colorimetric detection of calcium ions with arsenazo III was described in the previous Chapter (Section. 2.4). Trying to miniaturize the process to fit the micro-scaled chambers of the chip, one can simply think of a reservoir with dimensions of few

millimeters or less, into which a sample containing Ca and the dye ASA III solution are injected from two separated inlets. It is expected to have a uniform mixture, which has a color corresponding to the concentration of the Ca^{2+} ions in the sample. This actually not happens as it occur in the macro-scale, due to the emergence of a number of novel phenomena in terms of *mixing* fluids and *filling* micro-channels. Handling these challenges in the field of micro- and nanofluidics has become an attractive research topic recently. In this Section we will take a look at possible solutions to these issues.

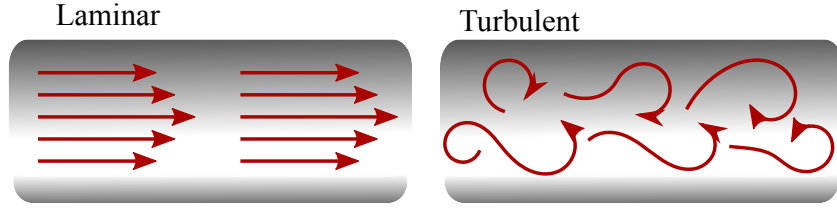


Figure 3.1.: Different types of flow in fluids

3.1.1. Microfluidic Mixing

Flow of fluids can be categorized into *laminar* or *turbulent*. While particles in laminar flow move along smooth paths in layers, turbulent flow is characterized as unpredictable and chaotic (Figure 3.1). To distinguish between these two types of flow, the dimensionless Reynolds number (Re) is defined as the ratio between inertial force and viscous force:

$$Re = \frac{\rho U^2 V}{\mu U S} = \frac{\rho U L}{\mu}, \quad (3.1)$$

where, ρ is the density, μ is the dynamic viscosity, U is the average velocity of the fluid and L is the characteristic length, that is, the ratio of the volume V of the fluid to the surface area S of the walls that bound it. Reynolds numbers below 10^3 denotes laminar flow. Above that, the flow starts to exhibits components of turbulence, that turns to complete chaotic flow for $Re < 10^4$. In microfluidics, due to the fine structure of the channels, complete laminar flows exist. This uniaxial movement of fluid layers becomes the main obstacle when mixing fluids; adjacent stream of fluids move forward along the channel and the only reaction between them occurs via *molecular diffusion* at their interfaces. A process that takes relatively long time to complete [69, 70]. In this regard, the diffusive mixing time, t_m , is defined as:

$$t_m = \frac{d^2}{D}, \quad (3.2)$$

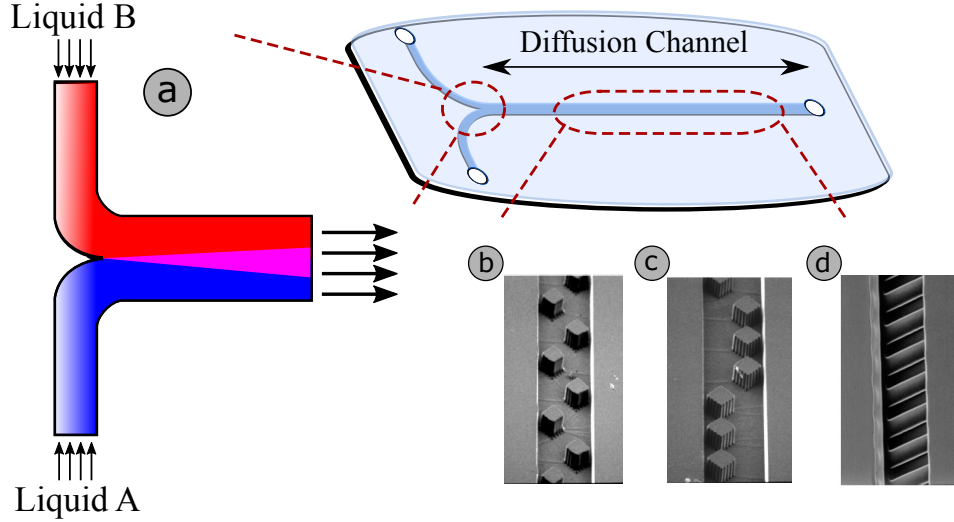


Figure 3.2.: A prototype of a T- micromixer a) the intersection between two liquids is shown in more details. Diffusion process mix up the red and blue fluids gradually along the channel b) and c) scanning electron microscopy (SEM) image of the obstacles introduced in the channel [71] d) SEM image of slanted grooves on the bottom of the channel to enhance the mixing process [72].

where d is the transverse diffusion length and D denotes the diffusion coefficient. To reduce the time of the process to a reasonable amount, diffusion length, d , should be kept small. However, factors such as photolithography resolution and available fabrication technology, set a limit in defining the minimum diffusion length and hence the entire geometry.

Required fast and controllable mixing of fluids encouraged the researchers to present new substitutions for slow diffusion-based mixing. These methods can be divided into two main groups [73, 74]:

In **active** micromixers an external source of power provides the required force to reach proper mixing. For example, Yang et al. [75] introduces an active micromixer that uses ultrasonic vibrations. A bulk piezoelectric ceramic is attached underneath a membrane. Excitation of the piezoelectric by a 60 Hz square wave, causes the membrane to oscillate, which in turn accelerates the mixing process of the liquids inside the mixing chamber above. Wang et al. [76] has also proposed acoustically induced gas bubbles into the chamber to enhance the mixing. Interactions with the acoustic field, causes the bubbles to vibrate and stir the fluids. Other active micromixers, utilize electrokinetic

effects [77], surface acoustic waves [78] or thermal mixing [79].

Passive micromixers rely merely on the configuration of the microchannels, that are designed specifically and innovatively to either increase the contact area/time between mixing species to elevate the inter-diffusion, or artificially rebuild the absent turbulent flow by means of chaotic mixing principles. In Figure 3.2, a T-type micromixer is shown. In its simplest form, mixing occurs gradually as soon as two liquids join in the channel. This relatively time-consuming diffusion process can be enhanced after modification of the channel, e.g., by introducing obstructions to break-up the flow [71], or embedded periodic barriers [72] within the channel. Other techniques such as split-and-recombine flow configuration [80], interdigital [81], zigzag patterned and multi-lamination geometries [82] are among highly regarded methods in the literature.

3.1.2. Filling Micro-channels: Phaseguide Theory

Appearance of air bubbles in the microfluidic channels and cavities is likely to occur while introducing the sample liquids. This incident can largely alter the results and should be avoided. Methods were suggested for proper filling of the micro devices, for instance, priming the device with carbon dioxide (CO_2) prior to filling is suggested by Zengerle et al. [83]. Due to solubility of CO_2 in water, gas bubbles disappear after filling. Selective change in wettability of the channels by modification of surface roughness is also presented by G. Takei et al. [84].

Here, we discuss a method, presented by Vulto et al. [85], that utilizes modification of the device geometry to reach perfect filling, based on capillary action. In this method, the liquid flow can be controlled by introducing photo-lithographically patterned obstacles, i.e., phaseguides, into the chamber. As depicted in Figure 3.4.d, the fluid front aligns itself to the phaseguide as a result of the *meniscus pinning* effect. This concept needs to be discussed in detail:

Depicted in Figure 3.3, hydrophilic or water-loving substrates are compared with hydrophobic or water-fearing substrate. This characteristic of a substrate is determined by the geometry of a water drop on its flat surface. In hydrophilic case the angle between a droplet's edge and the surface, i.e., contact angle, is less than 90° . For hydrophilic materials the contact angle is larger than 90° .

In a narrow channel with hydrophilic walls, the adhesion force between the liquid particle and the walls is higher than between the liquid itself. This effect causes the formation of a concave meniscus at the interface between air and the liquid. While

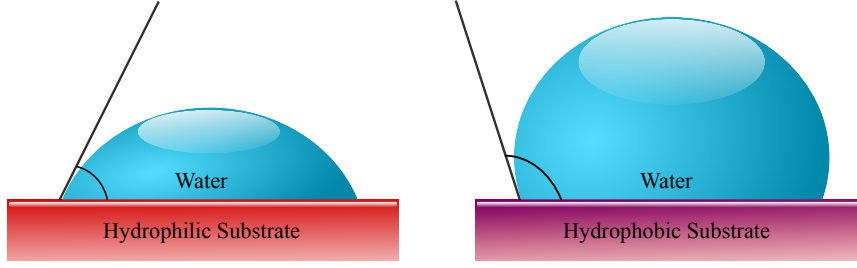


Figure 3.3.: Comparison between two different surfaces in terms of wettability. A water drop on a hydrophylic substrate has much smaller contact angle comparing to hydrophobic substrate.

attraction force from the wall tries to increase meniscus depth, surface tension of the liquid acts to reduce the area of the interface leading to the advancement of the fluid in the micro channel. This effect is known as capillary action. To relate the capillary effect to the surface tension, Young-Laplace pressure drop, ΔP_1 , over the interface between air and liquid can be calculated as follows:

$$\Delta P_1 = \frac{2\gamma}{h_1} \cos \theta_1, \quad (3.3)$$

where, γ , is the surface tension, h_1 is the height of the channel and θ_1 is the contact angle (Figure 3.4.a). When the fluid reaches the barrier, as depicted in the Figure 3.4.b, height of the channel as well as the contact angles changes depending on the wettability and the geometry of the hydrophilic channel. The new value for the pressure drop becomes:

$$\Delta P_2 = \frac{\gamma}{h_2} (\cos \theta_1 + \cos \theta_2) \quad (3.4)$$

Reduction of the channel height, h_2 , introduces a variation in pressure drop at the interface. Naturally, the fluid “chooses” the path with minimum pressure drop, that is, the meniscus pinning to the barrier and advancing along the phaseguide but not over it. Utilizing this technique, the microfluidic cavities could be filled with patterned phaseguides in a way, that the flow advancement becomes fully controllable, preventing bubble encapsulation at dead angles. The calculated pressure drop for hydrophilic channels has a positive sign. On the contrary, in hydrophobic channels the Young-Laplace pressure drop has a negative sign, which means the liquid doesn’t show tendency to fill the channel by itself, hence external pressure should be applied [84].

Perfect filling and emptying of chambers, requires a further step to handle the overflow of the fluid at certain positions. Taking into account the fact that overflow occurs at the

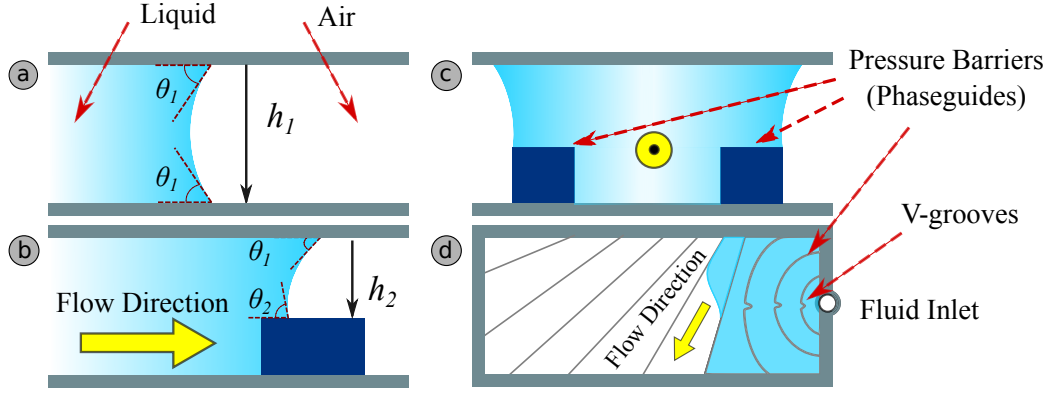


Figure 3.4.: a) Liquid flow in a hydrophilic channel is shown b) reaching the barrier, the reduction of height and change in the contact angles differs the Young-Laplace pressure drop at the air-liquid interface c) naturally, fluid advances along the path with minimum amount of pressure drop, i.e., a path along the barrier to which the fluid is pinned without crossing it d) yellow arrow shows how the fluid advances along the phaseguides in the microfluidic chip. The patterned surface of the chip, is divided into several segments. Complete filling of the chip can be achieved, by controlling the overflow of the fluid in certain spots to reach the next segment. This is done by designing V-grooves or sharp contact angles at the points, where overflowing is intended. (Images recreated from [85,86])

smallest phaseguide-wall angles, will make the process control feasible by introducing a sharp bending or branching structure within the barriers at the suitable places or by adjusting the contact angles to form a so-called V-groove at the walls (Figure 3.4.d) [87]. For this thesis, we are interested in the *confining phaseguides*, that serve as a boundary of the liquid without any planned overflowing spots.

3.2. Chip Design

All the concepts discussed so far will be employed in the manufacture of a microfluidic chip, which provides a fast and inexpensive point-of-care testing platform. The chip consists of 16 reaction chambers, structured with dry film and sandwiched between two glass slides. Each rectangular chamber, depicted in Figure 3.5, is divided into reagent segment and sample segment, separated by means of the so-called capillary pressure barriers (phaseguides) as mentioned earlier. Reagent segment is a comb-shaped

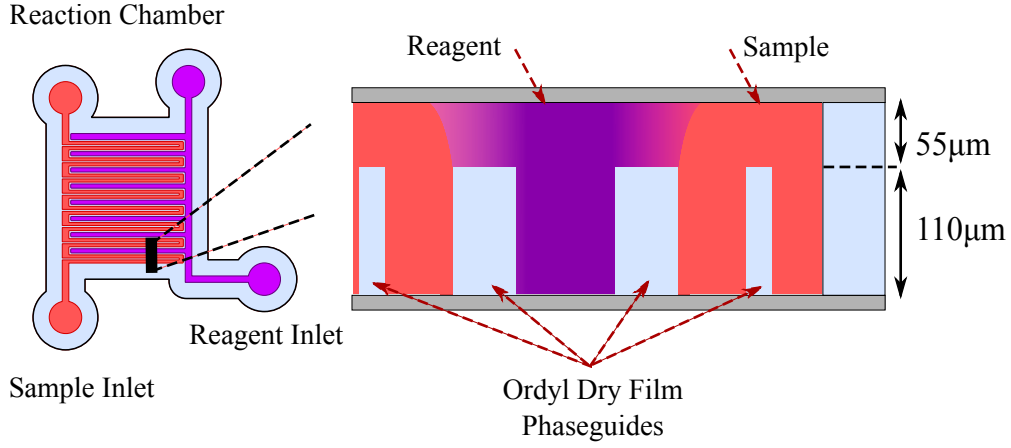


Figure 3.5.: A reaction chamber and its cross-sectional view is illustrated. Initially, the reagent (violet), containing hydrogel, calcium sensitive dye ASA III and masking agent, is injected into the reagent inlet of the chamber. Polymerization of the hydrogel under UV light or by cooling down, forms a solid structure capable of maintaining the dye into its network. Next, the sample (red) is injected into the microchannel meandering around the finger structured hydrogel. After around 2 minutes, diffusion of the sample into the hydrogel network and binding with the ASA III, will cause a detectable change in its color.

structure that is to be filled with a mixture of the ASA III, masking agent and hydrogel (Chapter 4) via the inlet hole. To maximize the contact area between two segments, the sample segment is patterned in shape of a meander path, embracing the outer side of the reagent segment. While filling, the reagent mixture is pinned to the barriers and advances along the phaseguides. If no overflow of the reagent occurs, in-situ polymerization of the hydrogel is performed. Solidified hydrogel enables flawless injection of the sample solution in next step, with no overflowing concerns. Two outlets are placed at the end of both injection paths for air evacuation. The optimum geometry is obtained with barrier height to chamber height ratio of almost $2/3$, to ensure appropriate guiding of reagents having different viscosities [88]. To achieve this geometry, two layers of dry-film on the bottom slide determine the barrier height and another layer on the top-slide increases the total height of the chamber to $165\mu\text{m}$. Fabrication steps will be presented in detail in the next Section.

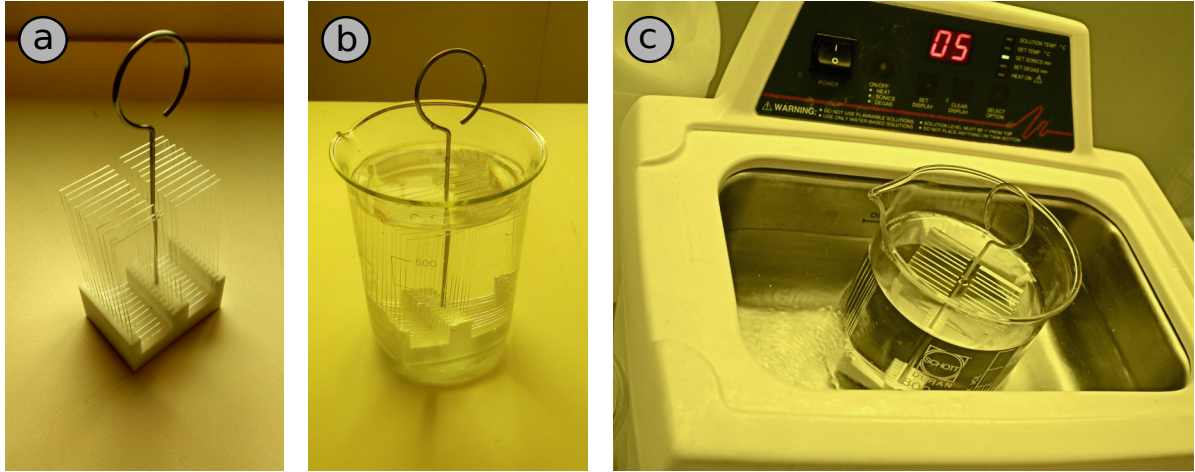


Figure 3.6.: Cleaning the slides before lamination a) slide holder is filled with glasses b) in the next step, the slide holder is submerged in a detergent solution containing RBS 50 c) the beaker is then put in an ultrasonic cleaner for 15 minutes.

3.3. Manufacturing Steps

Microfluidic chips can be fabricated by means of a fast and low-cost prototyping technology by means of dry film photoresists. Here, the manufacturing process of microfluidic chips using a $55\text{ }\mu\text{m}$ thick negative dry film resist Ordyl SY355 (*ElgaEurope, Italy*) is presented. The process steps can be divided into structuring two glass slides separately and bonding them together in the final step. The slide on the top, contains powder-blasted fluid inlets and outlets and $55\text{ }\mu\text{m}$ thick structures. This is referred to as the top slide or the $55\text{ }\mu\text{m}$ slide. To increase the thickness of the structures to $110\text{ }\mu\text{m}$ on the bottom slide, a second layer of dry film is laminated. Chips are fabricated on standard glass microscope slides ($76\text{ mm} \times 26\text{ mm} \times 1\text{ mm}$). Fabrication steps are explained separately for bottom and top slide as follows.

3.3.1. Bottom Slide

The $110\text{ }\mu\text{m}$ bottom slides contain the delicate micro-channels. To increase the efficiency of the fabrication, these steps should be carried out accurately in a clean environment. A tiny dust particle that comes in contact with the structure, can block the entire channel and prevent proper filling of the chip. Structuring the bottom slide is summarized in Figure 3.7.

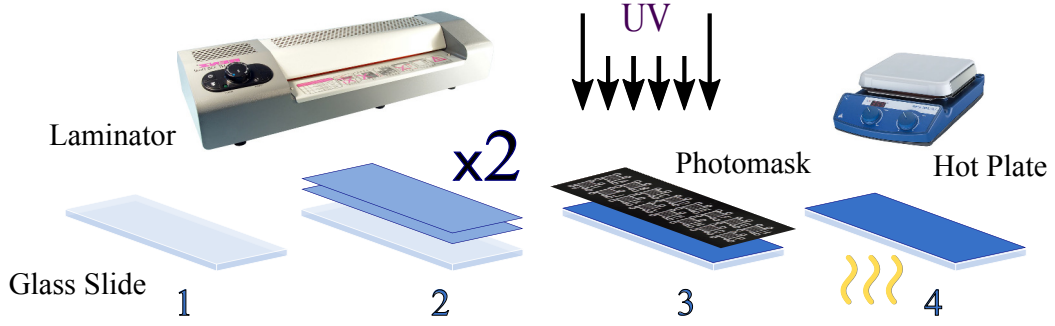


Figure 3.7.: Fabrication of the channel structure on the bottom slide, 1) glass slides are cleaned and completely dried, 2) two successive layers of Ordyl dry film resist are laminated one after another on a glass slide using an office laminator, 3) photolithography mask is placed on the slide and affixed with glue at both ends, UV exposure for 15 seconds is carried out 4) a post-exposure bake for 50 seconds on a hotplate at 85 °C is also required before the developing step.

Cleaning the glass substrates To ensure good adhesion of the Ordyl photoresist and increase the efficiency of the end products, first step is to clean the glass slides. This is done by RBS 50 solution (*Sigma-Aldrich, USA*) which is a detergent for laboratory glassware. A slide holder is filled with glass slides (Figure 3.6.a) and immersed thoroughly in a beaker containing a mixture of 5% RBS 50 in DI (deionized) water (Figure 3.6.b). Next, the beaker is placed in an ultrasonic cleaner (*Branson 2210 DTH, USA*) for 15 minutes (Figure 3.6.c). To wash the RBS 50 away, this step needs to be repeated for another 15 minutes in DI water. For drying the glass slides afterwards, they need to be kept vertically in a slide rack in a clean environment for about an hour.

Hot roll lamination of the photoresist For lamination, a hot roll office laminator (*Renz HT 330L, Germany*) is used. The rolls should be warmed up to 90 °C prior to use. A piece of thick print paper (160 – 200 g/m²) is used as a carrier, on which the cleaned glass slides are placed next to each other. Depending on the device, up to 7 slides can be laminated at once (Figure 3.8.b). When thicker structures are desired, successive layers can be laminated on a single glass slide. Dry film strips with a width of 11 cm are cut from the Ordyl roll. The length of the strip remains as it is.

Ordyl dry film has a protective layer on each side. One surface is covered by a polyester (PET) and the other is protected by a polyethylene (PE) layer. The PE layer is easier to peel off and blurrier compared to the PET layer [85]. To distinguish between

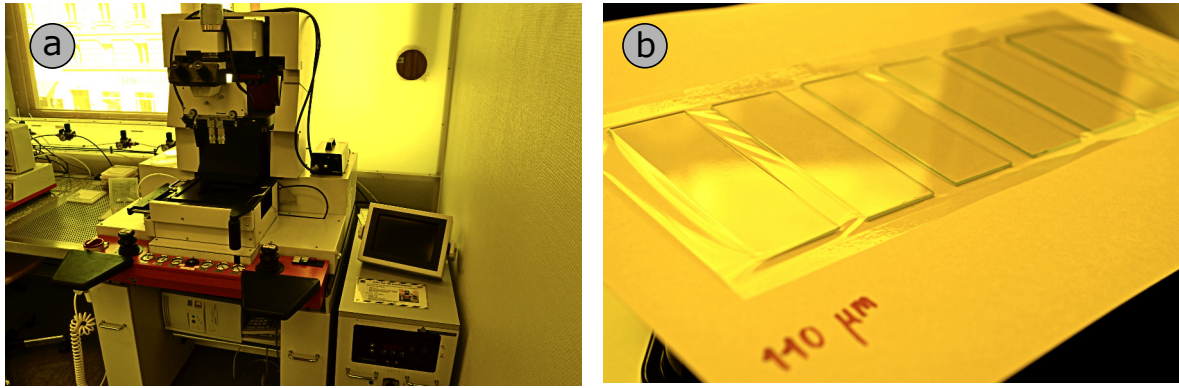


Figure 3.8.: a) Mask aligner used for the UV structuring of the Ordyl film b) laminated slides on a carrier paper.

the protective layers, the curvature of the Ordyl strip after cutting from its role, should be noticed. The concave surface is covered by PE layer, that needs to be removed prior to lamination. The PET layer is either removed prior to the second layer lamination, or remains until the last step before developing.

A post lamination bake on a hot plate for 3 minutes at 70°C is necessary to ensure better adhesion of the Ordyl film on the glass slide. Laminated Ordyl layer is then cut along the glass edge by means of a sharp scalpel. The glass slides with 110 μm of Ordyl dry film resist, are now ready for UV exposure.

UV Exposure Photolithography plastic masks (*Zitzmann, Germany*) are used to structure the Ordyl film. Exposure for 15 seconds using a mask aligner (*Karl Suss MA 150, USA*) (Figure 3.8.a) causes the exposed areas to remain on the surface, while the rest becomes solvable in the developer solution. It is essential to hold onto the right timing of the UV exposure. Overexposed chips can not be developed properly in the developer solution and usually should be discarded. Underexposed structures are also vulnerable to the developer agent and can be washed away. After detaching the second protective PET layer, a post-exposure bake (PEB) is carried out for 50 seconds at 85°C.

Developing Ordyl SY Developer (*Elgaeurope, Italy*) is a mixture of 2-butoxyethyl acetate and xylene at volume ratio of 7:3, respectively. A diluted version of the same mixture with 70% xylene (*Sigma-Aldrich, USA*) is used as rinsing medium to clean the structure from dirt with no considerable further developing. Developer and rinse need to be handled with caution. The solutions are skin irritant and inhaling their vapour can

cause dizziness and headache. Therefore, wearing gloves and a gas mask is necessary.

Four glass dishes should be prepared, as depicted in Figure 3.9.a. First, a round glass petri dish (150 mm) is filled with developer up to one-third of its height. We used large size petri dish to save time by developing multiple slides at once. In order to limit the casual movements of the slides while rotating on the shaker, therefore to prevent overlapping and scratching of the slides, another smaller dish is used to block the center of the dish, as shown in Figure 3.9.c.

Second dish is filled with Ordyl Rinse, enough for one slide to be immersed thoroughly. The third dish is filled with isopropanol and the last one with DI water. Glass slides with 110 μm of exposed Ordyl on them are immersed into the Ordyl Developer in the first petri dish. Next, the dish is placed on a digital orbital shaker (*IKA Rocker 3D, Germany*) for 9 minutes with a rotational speed of 25 rpm. Best uniformity of developing step can be achieved, by changing the orientation of the slides, once 4.5 minutes of the developing time is passed (Figure 3.9.b). After several times of developing, the Ordyl Developer becomes contaminated by small residues of the insoluble dry film and needs to be replaced.

The slides are then picked with a wafer handling tweezer and dipped into the Ordyl Rinse for 20-30 seconds. Gently rotating the dish with hand is enough for this step. Next, the slides are immersed in isopropanol for 1 minute to help clean off the greasy remains from the surface. Finally, they are put into the dish filled with DI water. To have cleaner slides, back side of the slide can be washed directly under the DI tap water (Figure 3.9.d). The slides can finally be dried on a cleanroom tissues (*Absormat CC448G, Clear & Clean, Germany*), for around two hours, or alternatively, on a hotplate at 70 °C for 10-15 minutes.

3.3.2. Top Slide

Compared to the 110 μm , the 55 μm thick top slides need a simpler structuring of the dry film, because it merely includes the boundary edges of each analysis chamber. Creating the inlet and outlet holes on the glass is, however, a time consuming task. Fabrication steps for the top slide are summarized in Figure 3.11.

Preparing Powder-blast Masks To create holes on the predefined spots on the glass, a powder-blast resist film (*Vinyl Sandblast Mask, Ikonics Imaging, USA*) serves as a mask. This pink mask itself should be first structured by another plastic photomask

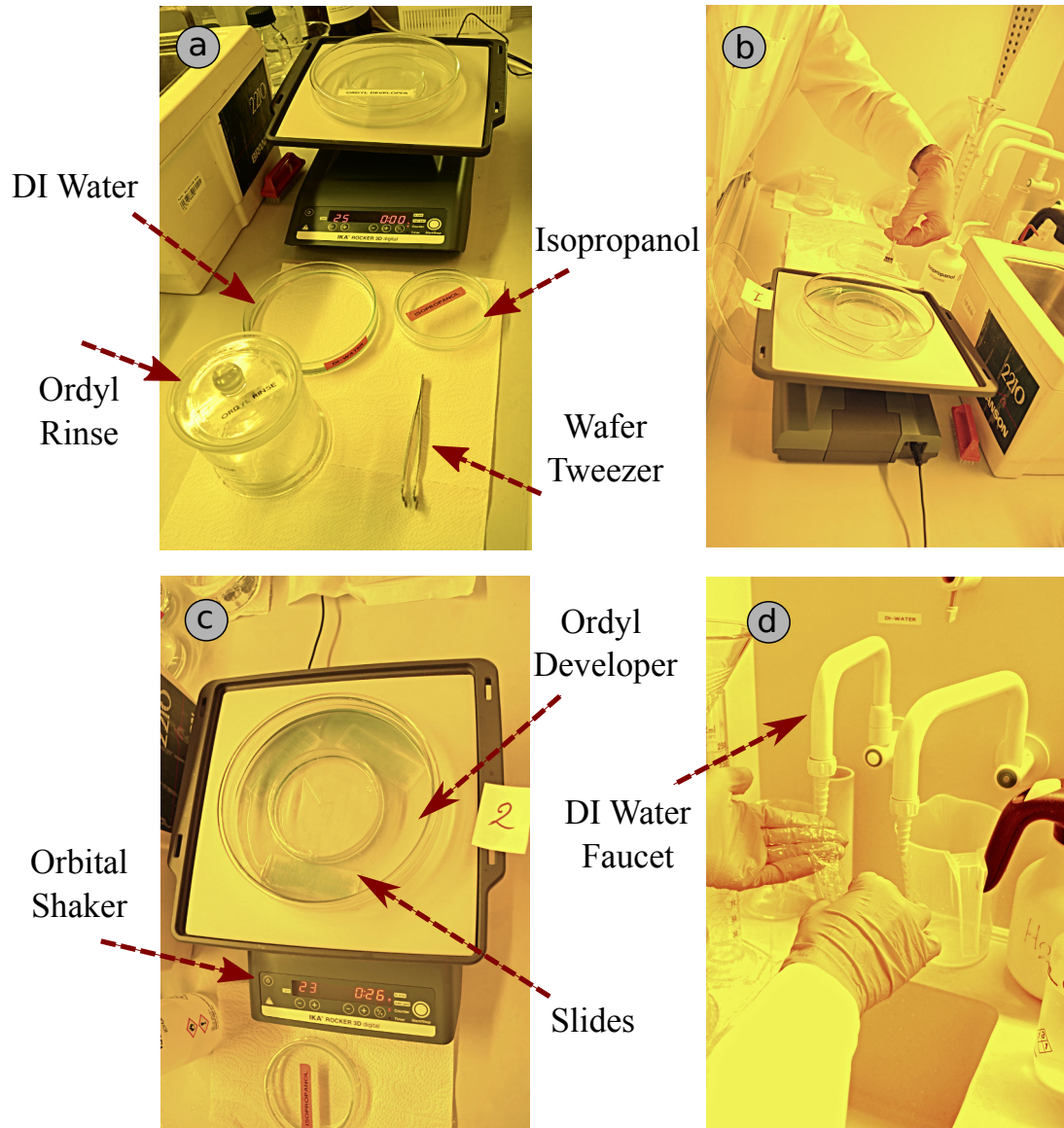


Figure 3.9.: Developing structured dry film a) required stuff to accomplish this step includes a digital shaker and four containers of Ordyl Developer and Rinse, isopropanol and DI water b) changing the orientation of the slides, while rotating on the shaker, results in more uniformly developed structures c) the center of the dish is occupied by another smaller dish, in order to restrict casual movement of the slides while rotating d) the slides, afterwards, will be rinsed in Ordyl Rinse, isopropanol and DI water, respectively. To further clean the backside of the slides, they can be washed carefully under the tap water.

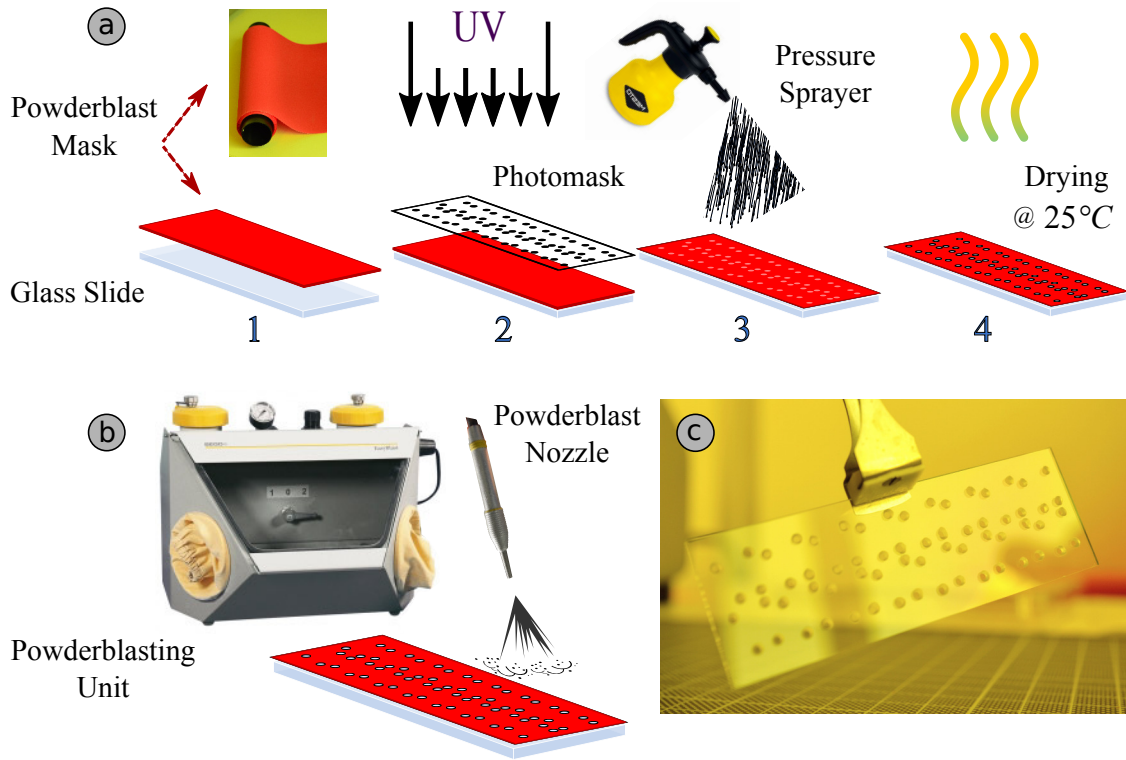


Figure 3.10.: a) Preparation of the powder-blast mask (pink mask) is comprised of: 1) glueing the resist onto the glass slide, 2) structuring with UV light, 3) developing under pressurized warm water (50 °C) and 4) drying at room temperature b) once it is structured, the pink mask can be used several times for powder blasting c) the final top slide with fluid holes after washing step.

(Zitzman, Germany) that defines the inlets and outlets. To perform this, the pink mask is cut from its role, to a size that matches the glass slide to which it is glued afterwards. The photomask is also glued at both ends to stick on the pink mask. UV light exposure for 6 seconds (*Karl Suss MA 150 Mask Aligner, USA*) causes the unmasked areas of the pink mask to become insolvable in water. Developing is done by washing out the film with hot water of around 50 °C pressurized by a one-hand pressure sprayer (*MESTO, 3132NG CLEANER*) and sprayed to the surface with gentle motion. Washout should be continued until the holes are appeared. The pink masks are placed on a clean room paper to dry overnight at room temperature. Dried masks have a uniform pink color and can be reused for powder blasting several times. Figure 3.10.a summarizes the steps needed to prepare the powder-blast mask.

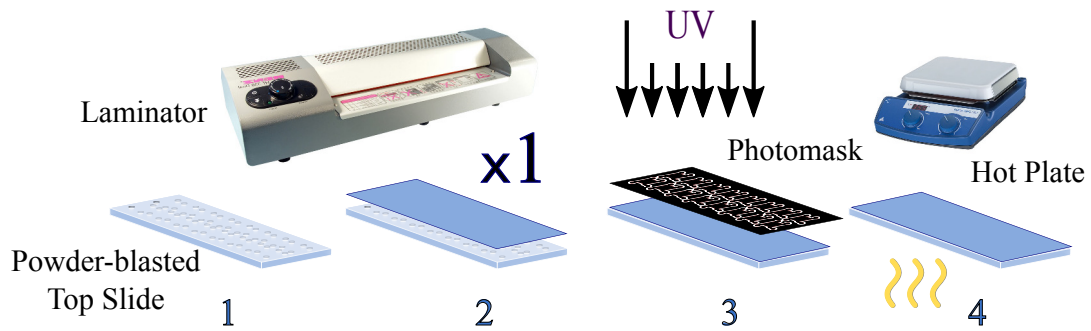


Figure 3.11.: Top slides are structured in almost the same manner as the bottom slides. The only difference is the powder-blasted slides used in this step and the single Ordyl dry film lamination.

Powder Blasting For each microfluidic chamber 4 holes need to be powder blasted using EasyBlast (*Bego, Germany*)(Figure 3.10.b). In this process, micro abrasives, in this case corundum grains with 99.8% aluminum oxide (Al_2O_3) (*Pluradent, Germany*), are accelerated to the glass surface with a blasting nozzle by highly compressed air. The grains have no effect on the pink mask, but penetrate to the glass through its holes. A vacuum cleaner (*KÄRCHER NT 35/1 Tact TE, Ludwig Müller GmbH, Austria*) is connected to the device in order to collect the corundum grains for reuse.

Cleaning powder-blasted slides In this step, the top slides are washed under the tap water for the remainder of the grains to be washed away. Next comes the removal of the pink mask, which should be done very carefully, since the slides are now brittle due to

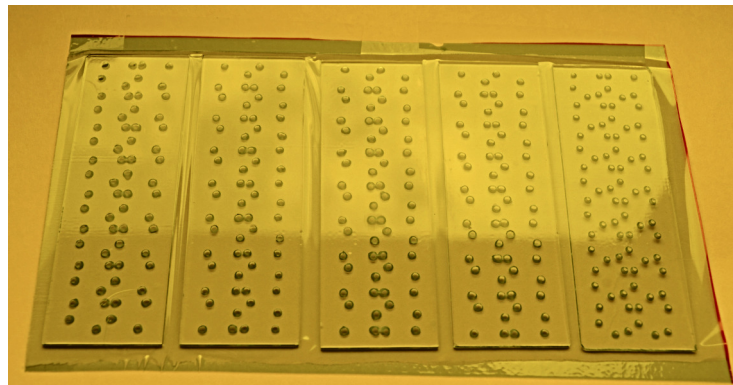


Figure 3.12.: Top slides with powder-blasted holes after lamination of a single layer of the Ordyl dry film.

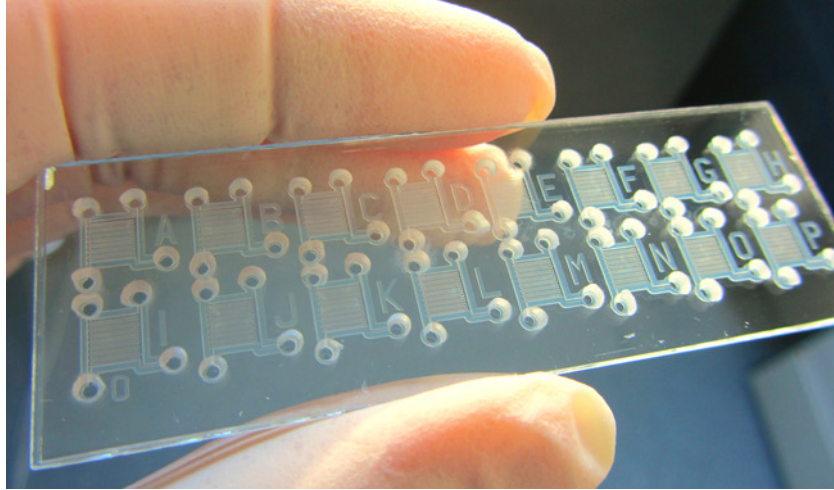


Figure 3.13.: The last step of fabrication is accomplished through bonding the top and bottom slides together. After visual alignment of the slides, they are pressed together with an adequate pressure on a hotplate at 150 °C. The microfluidic chip can then be used after several minutes of cooling down.

the many holes. The pink masks can be washed and dried for next use. The cleaning process of powder-blasted glass slides is identical to the steps described in Section 3.3.1. An extra washing with DI water for 15 minutes in ultrasonic bath is needed prior to washing with RBS 50 solution to remove glue residues and stuck abrasive grains. A top slide with holes after accomplished cleaning step, is shown in Figure 3.10.c.

Lamination, UV Exposure and Developing The rest of the fabrication process is identical to the bottom slide, except for the thickness of the Ordyl film which is 55 μm . In this regard developing time decreases to 5 minutes for each slide. The UV exposure in this step needs now more accuracy in terms of alignment between the inlet/outlet holes and the exposure mask. Figure 3.12 shows the undetached laminated top slides on a carrier paper.

3.3.3. Bonding

Before bonding two structured slides together, they should be checked under microscope whether the channels are clean and properly developed. Even with careful execution of the fabrication steps, the average efficiency hardly exceeds 50% for bottom slides.

However, the efficiency is higher for top slides and could reach up to 80-90%, due to their simpler structure. After choosing two matching slides, they need to be aligned by eyes. Once the best alignment is reached, the two slides are pressed to each other by fingers and placed on a hotplate at 150 °C for 5 seconds. Continuous pressure is needed perpendicular to the surface of the chip to ensure proper adhesion. The microfluidic chip is ready for use after cool down at room temperature (Figure 3.13).

4. Measurements and Results

The manufactured microfluidic chip is utilized in the colorimetric analysis. Results from the measurements in this step are expected to provide an estimation of the amount of calcium in human milk. Typical Ca determinations are accomplished in a cuvette, requiring 1-3 mL of the reagent. Miniaturizing the experiment allows for the complete execution of the measurements in a micro scaled chamber, that can be filled with reagent volume as low as 5 μ L. Apart from low reagent and sample consumption, easy implementation of determination steps enables inexperienced personnel to accomplish the task after a short instruction. This is a big step forward in realizing the goal of this thesis; fast and reliable in-situ evaluation of human milk in NICUs. Beside all challenges discussed so far to scale down the assay, it is the vital role of the *hydrogel*, that makes the miniaturization procedure feasible.

4.1. Hydrogel Concept

Hydrogel is a network of hydrophilic polymers that have intensive water absorbing nature. Their ability to retain high amounts of water or aqueous solutions in their three-dimensional structure, has triggered their wide range of application in industry and research activities. Generally, presence of three terms is required in synthesizing hydrogels; monomers, initiators and cross-linkers [89]. Understanding the formation mechanism of this polymer network is required to control hydrogel structure and properties for specific applications. A short review on hydrogel synthesis and properties is presented in the following.

Preparation There are many types of hydrogels, prepared for specific applications with various techniques. A hydrogel network may be formed from polymers, i.e., macromolecules consisted of large number of repeated units (monomers). The polymer chains in turn, link together to form a single giant molecule, the so-called *gel*. The process of establishment of cross-links between the polymer chains is called *gelation*. During gela-

tion, the substance experiences a phase transition to reach the gel-phase. In this state, the gel is able to swell with water up to hundredfold of its own mass, without being dissolved. This is due to the fact, that linkage of the polymer chains is not point-to-point, but occurs at certain points via cross-linkers. This results in formation of a network, consisting of void spaces between macromolecules that can bear huge amounts of water molecules [89–91]. Figure 4.1 depicts a simplified scheme of the hydrogel formation.

Depending on the cross-linking type, hydrogels can be categorized in two classes.

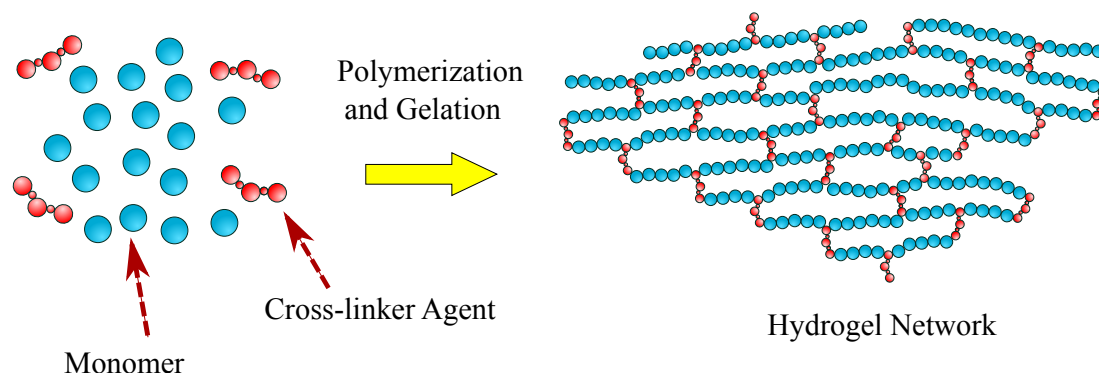


Figure 4.1.: Formation of hydrogel structure from monomers and cross-linkers.

Monomers, in the first place, attach to each other to create a long chain of polymer. In the illustrated example, cross-linkers create covalent bonds between polymer chains, in a manner that forms a network with vacant spaces. These spaces can be filled with molecules.

Chemical gels include covalently crosslinked polymers, while **physical gels** summarize all gel types with non-covalent crosslinks. The gelation of the latter may consist of hydrogen bonds, charge interaction between polymer chains with opposite charges or chain entanglement. Connections between the chains in physical gels are weaker compared to the covalent bonds of chemical gels. The result is formation of a reversible gel, with links that can be broken, for example by temperature increase.

Chemical gels, on the other hand, are permanent and mechanically more stable. They include number of cross-linking methods, such as free-radical polymerization, chemical reaction of complementary groups, UV irradiation or enzyme addition [91,92].

Applications Hydrogels can be formed in a manner, to become sensitive to certain environmental effects. These *smart* hydrogels exhibit changes in their physical properties in response to external stimuli such as pH, temperature, pressure, electrical and magnetic fields, ionic strength and certain molecular species. In this regard, hydrogels

have been proven to be promising materials in realizing micrometer-scale sensors and actuators based on MEMS techniques. For example, Gerlach et al. [93], make use of two pH- sensitive hydrogels, poly(vinyl alcohol)/poly(acrylic acid) (PVA/PAA) to fabricate a pH sensor. The swelling ability of the hydrogel blend is shown to be maximum in basic environment and minimum in acids. Volume change of the hydrogel in contact with different solutions, deflects a silicon membrane, which can be detected by a piezoresistive transducer. This way, an electrical signal read-out can be assigned to the pH value of each solution under test. Another ultrasensitive pH sensor, developed by R.Bashir et al. [94], structures a layer of hydrogel, consisting of poly(methacrylic acid) (PMAA) and poly(ethylene glycol) dimethacrylate on top of a silicon cantilever. Volume change of the polymer layer in accordance with the solution pH, bends the cantilever. In the dynamic range of the sensor, pH between 5.9 to 6.5, optical based deflection measurement systems can detect a pH change of $5 \cdot 10^{-4}$ for 10 nm deflection of the cantilever (Figure 4.2). Self-regulated flow control in microfluidic channels is another application of hydrogels.

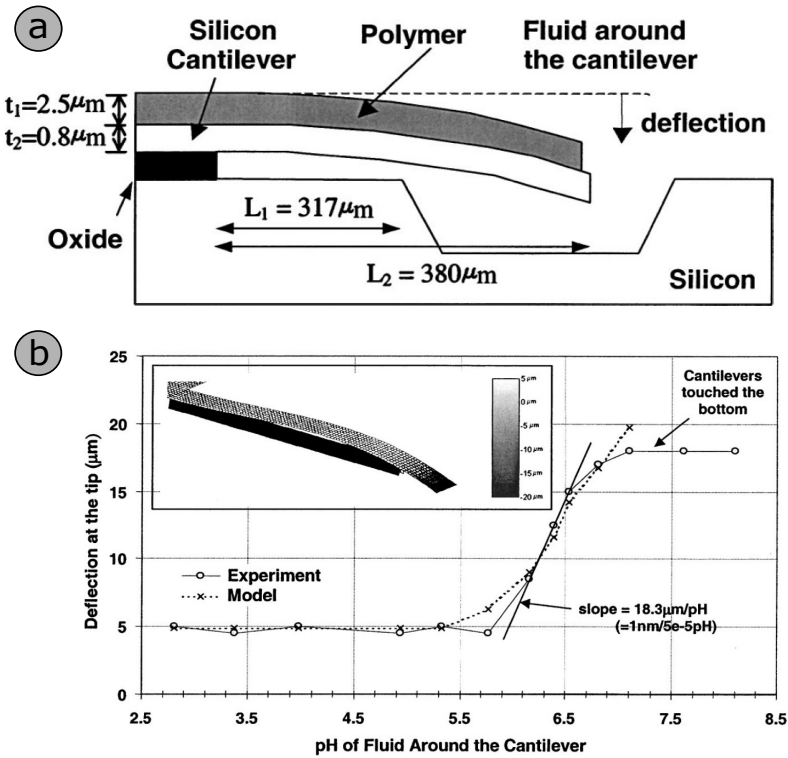


Figure 4.2.: a) Cross-section image of a Si cantilever with a layer of hydrogel on the top b) deflection of the tip versus pH value of the solution including the sensor, shows a step change of the cantilever between pH 5.9 and 6.5. Image adopted from [94].

D. Beebe et al. [95] has reported a hydrogel-based valve, with the ability to direct flow in certain branches in response to the liquid pH. As depicted in Figure 4.3, two different types of hydrogels are fabricated, by means of injection of the pre-gel solution followed by in situ photo-polymerization in the certain spots. One hydrogel valve is prepared to swell in contact with acidic environment and the other is sensitive to basic solutions. For liquids with pH value in the range 5.7–6.8, both branches are sealed (center image). Out of this range, there will be only one possible path for the fluid at a time, depending on its pH. Utilizing hydrogels in micrometer-scale devices, eliminates one of the main issues with these substances; their inherent low-response time improves noticeably as a result of down-scaling [95, 96].

In its swollen state, hydrogel matrix can still allow diffusion of other solute molecules,

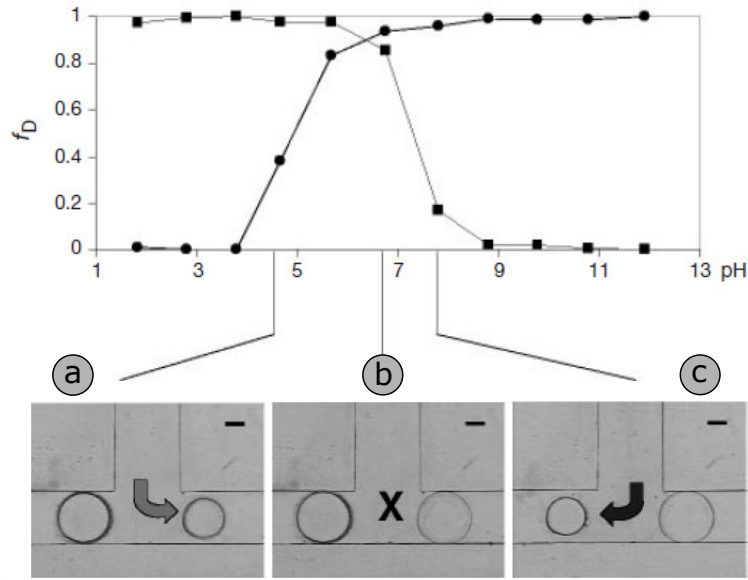


Figure 4.3.: The graph shows the fractional changes of hydrogels in diameter (f_D) depending on the pH value a) in acidic environment, the hydrogel gating the left branch swells and blocks the channel while the other shrinks and directs the fluid b) for pH value 6.7 both hydrogels are swelled and block the channels c) basic solution will be directed to the left branch after the right hydrogel gating blocks the channel. Image adopted from [95].

that rest in its network without any chemical interactions with the host molecules [90]. This unique characteristic of hydrogels has given rise to many biological, pharmaceutical and diagnostic applications. Many researches on hydrogel applications have been conducted in recent year in scope of tissue engineering, drug delivery, etc. [97].

Natural and Synthetic Hydrogels From origin point of view, hydrogels can be classified as natural and synthetic materials. The natural hydrogel used in this work is *agarose*, that takes its origin from seaweed. Agarose gel has been long in use in biological experiments, such as electrophoresis, to separate charged molecules according to their weight [98]. It is also among frequently reported hydrogels in microfluidic devices in recent years. For example, D. Puchberger-Enengl [99] has presented a microfluidic platform to culture live cells suspended in agarose gel.

Agarose is available in form of powder or tablets. Depending on the application, required volume of the substance is dissolved in DI water or other buffers such as TAE (tris-acetate-EDTA) or TBE (tris-boric acid-EDTA). Dissolving is carried out in high temperature, which is usually done in microwave or on a hotplate. The gel structure is formed after cooling the solution down to below gelling temperature [100].

4.2. Miniaturized Colorimetric Calcium Determination

To run the colorimetric experiments on the chip, the measurement setup in Figure 2.7 should be modified. This is done by replacing the cuvette-holder with a self-made device, specially designed for measurements on the microfluidic chip. As shown in Figure 4.4, the substituted device is assembled on an aluminium optical breadboard (ThorLabs, USA). Four mounted aluminium legs and a column, are adequately high, in order not to violate the *bend radius* of the optical fiber patch cords (OceanOptics, HALMA PLC, UK). While utilizing these cords (600 μm core size), the radius of the bending curve should not exceed 12 cm, otherwise it will cause microscopic fractures in the fiber and hence, error in the results [101].

Reagent and Sample Preparation To prepare the color reagent stock solution, ASA III powder (Sigma Aldrich, St. Louis, USA) is dissolved in its buffer. The optimum concentration of the color reagent, has been found out experimentally to be 6.48 mg/mL. Higher amounts of the ASA III forms unwanted precipitate in the solution. Buffer of pH 8.5, consists of 50 mM boric acid (H_3BO_3), 50 mM potassium chloride (KCl) and 10.1 mM sodium hydroxide (NaOH). As mentioned before (Section 2.4), to obtain the highest absorption, pH value of the color reagent should be about 8.5 – 9. Adjusting the pH is possible by gradual addition of boric acid (sodium hydroxide), in case, the measured pH value is still higher (lower) than expected. Monitoring the pH value is done by means of pH test strips. The same buffer is used to dissolve 8HQS to reach final

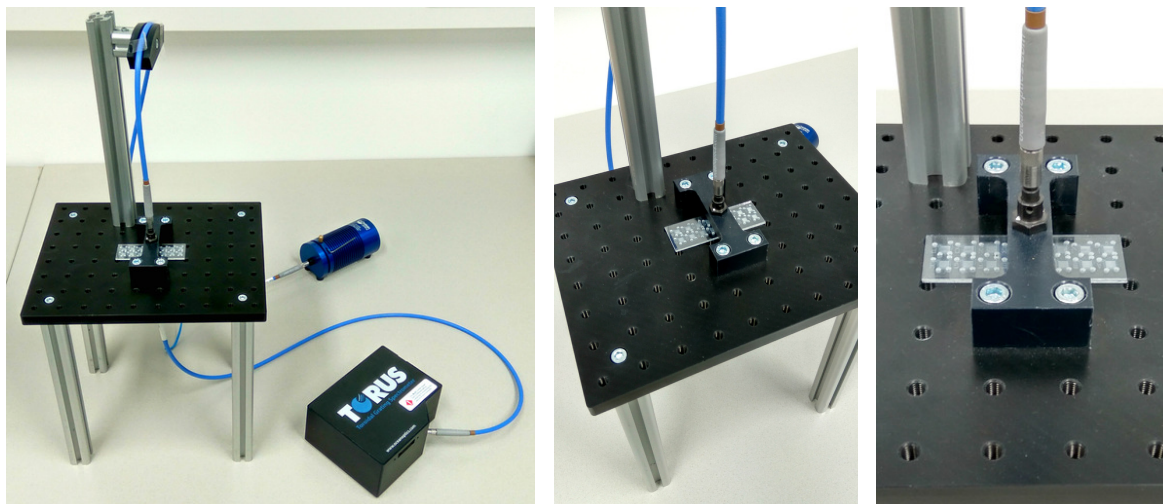


Figure 4.4.: Specially designed holder enables the colorimetric analysis with microfluidic chip.

concentration of 1.13 mg/mL of the masking agent.

Hydrogel is prepared from 0.5wt% agarose low melt (Carl Roth GmbH, Germany) in DI water. The solution is stirred and heated on the hotplate up to 90 °C until it dissolved completely. The gel solution is cooled down to 45 °C, but it should be kept above the gelation temperature (26 °C) prior to injection to the chip. Agarose solution, 6.48 mg/mL ASA III color reagent and 1.13 mg/mL 8HQS solution are mixed together in a conical tube and vortexed. 5 μ L of the mixture is injected to each reaction chamber of the chip using a pipette (Eppendorf Research plus, Hamburg, Germany). The chip is then kept in the fridge, in order to be cooled down to 4 °C for the formation of the gel and stabilization of the color reagent.

Human milk samples were provided by the Vienna General Hospital (AKH) from mothers of preterm babies. Within 24 hours of collection, the samples are homogenized to reduce the size of the fat droplets inside the milk that cause scattering of the incident light [102]. Homogenization procedures consists of immersion of the milk bottle in ultrasonic cleaner with pre-heated water (38 °C) for 30 minutes and vortexing the bottle for extra 30 seconds. The samples are then aliquoted into 1 mL conical tubes and frozen. Prior to analysis, the milk samples are thawed at room temperature and homogenized again.

Measurements and Results Figure 4.5.a displays the chip after the injection and gelation of the reagent. Prior to the analysis of HM samples, the functionality of the

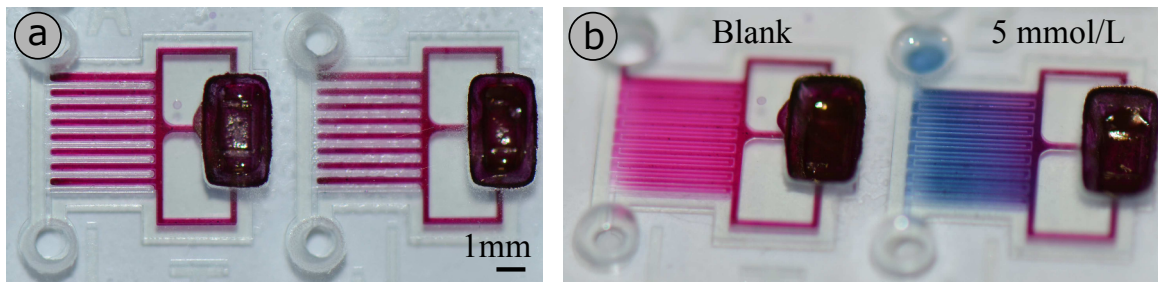


Figure 4.5.: a) Chambers, filled with reagent mixture, are ready for analysis b) emerged color after injection of the Ca sample solution (5 mmol/L) exhibits significant change comparing to the blank sample. Image adopted from [103].

color reagent was tested with a series of Ca solutions. Figure 4.5.b displays the color difference of the blank and 5 mmol/L of Ca solution. Having the chip available, the major task is now to prepare the standard curve. As mentioned before, standard curves should be prepared with series of diluted solutions with known concentration of the substance. Preparation of a standard curve from human milk samples, however, requires prior data on Ca content. Providing this data by other methods such as flame atomic absorption spectroscopy (FAAS) [104] is far from practical. To overcome this issue, the idea is to use human milk fortifiers (HMF) instead. HMFs, e.g., the one we used in this work, Aptamil FMS (Milupa, Bad Homburg, Germany), are standard additives prescribed in some cases, to elevate the nutritional value of breast milk and compensate its deficiencies. Formulated based on HM nutrient values (Appendix A), fortifiers are the best available alternative to human milk for preparing the standard curve. To accomplish this, a serial dilution of the HMF is prepared in conical tubes, 5 μ L of each is injected into the reaction chambers of the chip. After 2 minutes of incubation time, diffusion of the sample into the reagent gives rise to apparent change in the color. Absorption is measured by spectrometer at 655 nm for each concentration and is then plotted accordingly. As expected, for concentrations above 3 mmol/L saturation of the curve is observed. Below this amount, applying the linear regression results in a best-fitting line with $R^2 = 0.998$ (Figure 4.6).

The average Ca content in breast milk is 5.5-7.5 mmol/L [105, 106], which is beyond linear region of our standard curve. To remain in the linear region, dilution of the milk sample is necessary. Being thawed to room temperature and homogenized, each sample is diluted with ratio 1:2 with DI water. After injection to the chip and incubation time of

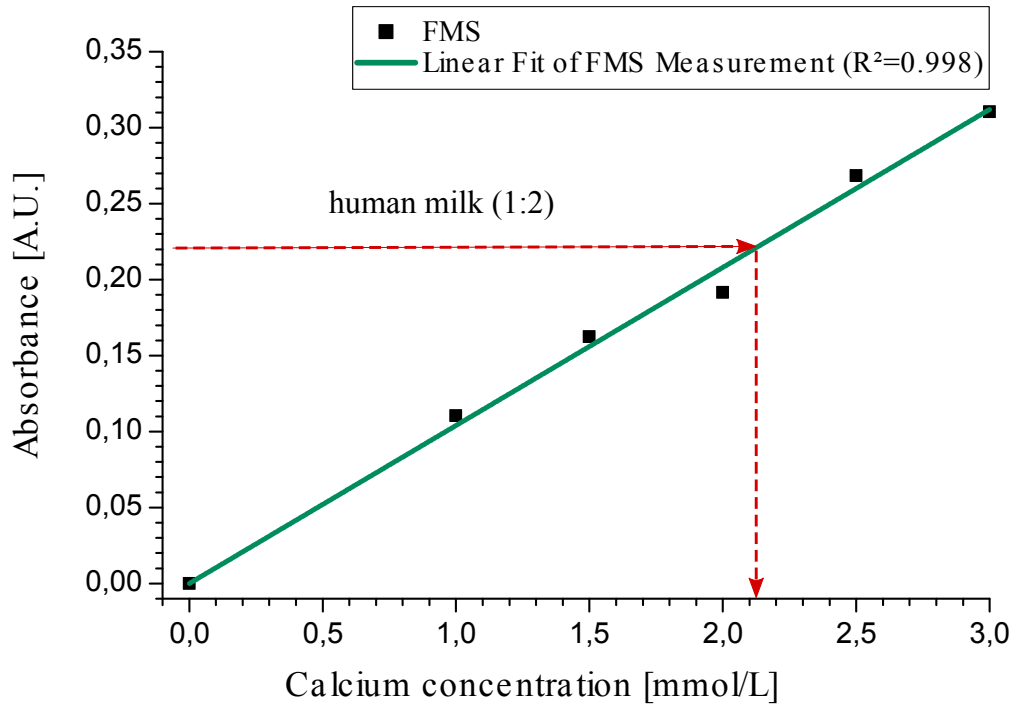


Figure 4.6.: Standard curve (green) is obtained from linear regression of acquired data points from spectrometer. Unknown concentration of the milk sample can be evaluated from this curve, when the absorption is available (red). Graph adopted from [103].

2 minutes, the absorption is measured. The red line in Figure 4.6 gives the concentration of the sample in accordance with the assessed absorption value. Due to the dilution ratio, the indicated value should be multiplied by 3, yielding the concentration of 6.4 mmol/L for the sample.

4.3. Discussion

Once the calibration (standard) curve is prepared, it can be exploited to evaluate many milk samples. The validity duration of the standard curves is not yet clear and needs to be assessed in a separate experiment. Few research has been conducted to investigate the expiry time of the standard curve for other substances [107,108]. If the Ca determination experiments are intended to take place repetitively, the time needed for refreshing the standard curve, i.e., the expiry date of the curve, should be provided in advance.

If the obtained absorption value is above the linear range, 3 mmol/L for our standard

curve, it will fall into the saturation region. In such cases, which often happens on the first try, we need a proper dilution of the sample. The right dilution ratio may take several trials to be determined. The extracted concentration should afterwards be modified relative to the dilution ratio. In order to gain reliable results, measurements should be performed in the same manner, as for standard curve preparation. During the chip fabrication, defects may be introduced to the products that have impact on the absorption of light. These minor influences are neglected in our analysis. But we need to follow the same recipe to prepare Ca indicator reagent (ASA III mixture) for both standard curve and the determination experiments. In addition, identical environment and facilities of experiments will increase the accuracy.

5. Outlook and Conclusion

Calcium content of the breast milk was successfully evaluated by means of a microfluidic chip. The initial aim of this thesis was to provide a fast and reliable measurement technique, to be applicable in neonatal intensive care units (NICU). To fulfill this goal, two essential factors should be taken into consideration:

- all the instruments associated with the discussed detection procedure, should be integrated into one single device,
- unskilled individuals should be capable of running the device and interpreting the results after a short instruction.

In this Chapter, we will discuss the challenges on the way of commercializing this detection technique. The results can then be expanded to embrace other chemical components, such as protein, lactose, phosphorus, etc., via modifying their colorimetric assays. The ideas presented in this Chapter are merely an attempt to investigate potentials in transition from research scope to industry, and are not included in our experiments for this thesis.

5.1. Compact Colorimetric Analyzer

A hypothetical instrument for determination of Ca concentration in a milk sample, can be as the one depicted in Figure 5.1.a. A filled microfluidic chip is inserted into the slot and results are shown for the unknown concentration after a few simple steps. Ideally, it is a battery-powered stand-alone device, with no need for other peripherals. In the following, we discuss the ideas to modify available instruments and exploit new technologies, in order to design this imaginative compact colorimetric analyzer.

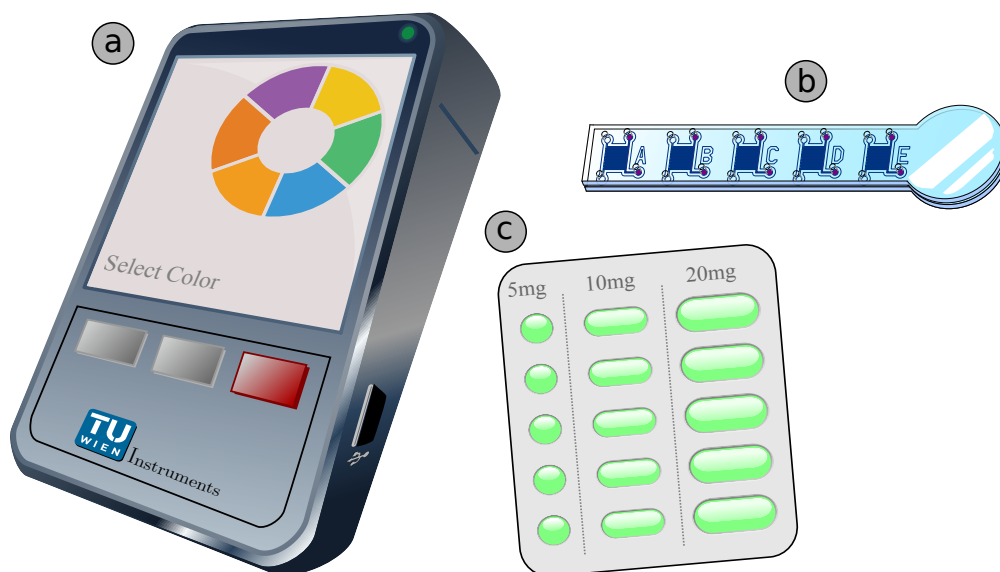


Figure 5.1.: a) The hypothetical device, that serves as a compact analyzer with ability to detect several substances based on colorimetric analysis. User will be asked to select a color from the color-wheel, that corresponds to the absorbing wavelength of the indicator and activates the related RGB LEDs on each chamber b) the modified microfluidic chip contains only 5 chambers. A set of 5 LEDs is embedded to emit light perpendicular to each chamber c) for easy and fast preparation of the standard curve, it is supposed that the required substances are available in form of tablets with precise volume. Solving tablets in certain amount of solvent will result in a serial dilution.

5.1.1. Modifying the Chip

The microfluidic chip, designed in previous chapters, is too large to be applicable to our compact analyzer. Hence, it can be optimized to contain a single row of 5 chambers (Figure 5.1.b). In case of Ca detection, these chips can be commercially available in suitable packages, with a pre-filled reagent segment, i.e., a mixture of ASA III, masking agent and hydrogel is already introduced to the chip and cured with UV exposure during the mass production. An expiry date needs to be defined for the product to ensure the best results. Depending on the compounds, preservation conditions, such as low-temperature storage and/or vacuum sealing can be applicable to extend the shelf life of the chips.

According to Section 4.2, for estimation of Ca content in human milk, the standard

curve is prepared from serial dilutions of human milk fortifier. To accelerate the analysis, the HMF can also be available in form of tablets with certain volumes in a blister pack. For instance, tablets can be in weights of 5 mg, 10 mg and 20 mg (Figure 5.1.c). If required, a combination of these portions can be used to make a new volume. For standard curve preparation, one needs to dissolve the tablets in a fixed volume of solvent and prepare the serial dilution, with no need to deal with scaling the dry substances. The pre-filled chips and the packages of the HMF, can be offered together as a *Ca analysis kit*.

5.1.2. The Compact Analyzer

After preparing the serial dilutions, they are introduced to the chip. After 2 minutes of incubation time, the chip is inserted into the device for analysis. To run the device for the first time, these sequential actions are assumed:

Mode Selection Once the chip is inserted, user interface of the device should automatically sense the chip and ask for mode selection. The instrument has two main modes of operation; first for preparing the standard curve and second for estimation of the Ca content (or any other chemical substance). After insertion of the chip for the first time, the standard curve preparation mode must be first selected.

Color Selection The user is also asked to select a color from the color-wheel. The colors are associated with the light emitting diodes (LED), embedded in the device as substitutes for the bulky light source. LEDs are available in different colors, each include particular wavelength range. Emission spectrum of a number of LEDs is depicted in Figure 5.2.a. Red LEDs, for example, have emission in the range 610 to 640 nm and can be selected for the Ca determination. Access to all colors in the color-wheel is possible, by utilizing multi-color LEDs. In this type of LEDs, new colors are achieved from combination of main colors (usually red, green and blue (RGB)), by applying proper voltage to the related pins (Figure 5.2.b and c). Alternatively, surface mounted device (SMD) LEDs can be used to save space (Figure 5.2.d and e). Depending on the number of chambers on the microfluidic chip, SMD LEDs can be mounted in a position perpendicular to each chamber. Proper housing of the LEDs can concentrate the emitted light and reduce scattering.

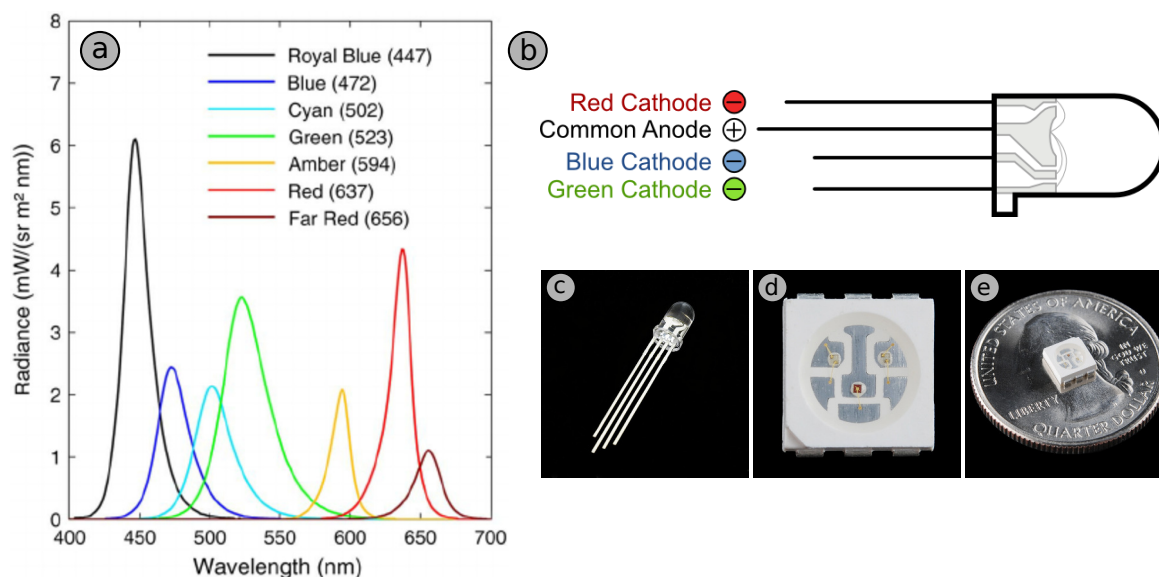


Figure 5.2.: a) Spectral power distribution of the light emitted by the color LEDs [109] b) and c) RGB LED is a type of light emitting diode with four pins. Applying voltage between the common anode pin and any of the color pins produces the indicated color. Simultaneous modulation of all three pins results in mixed colors [110,111] d) and e) surface mounted device (SMD) LEDs are alternative solution for producing desired colors in smaller dimensions [111].

Standard Curve Preparation In standard curve preparation mode, the device outputs the graph according to the acquired data and with the aid of its internal software, that provides the corresponding trend line and the coefficient of determination (R^2). The device should provide information about the linear interval of the graph as well. Values below or above this interval should be tagged as “out of range”. This occurs when the concentration is too low to be estimated, or, the concentration is high and falls on the non-linear part of the standard curve. The provided standard curve can be stored in the internal memory of the device along with the date of preparation. The device can be adjusted to remind user after a certain period of time for renewal of the standard curve.

Calcium Determination Second round of the measurement is achieved by selecting the Ca content determination mode. Several diluted versions of the milk sample can be prepared, each introduced to the chambers and inserted to the device. The dilution ratio should also be asked for each chamber, since it should be taken into consideration for the

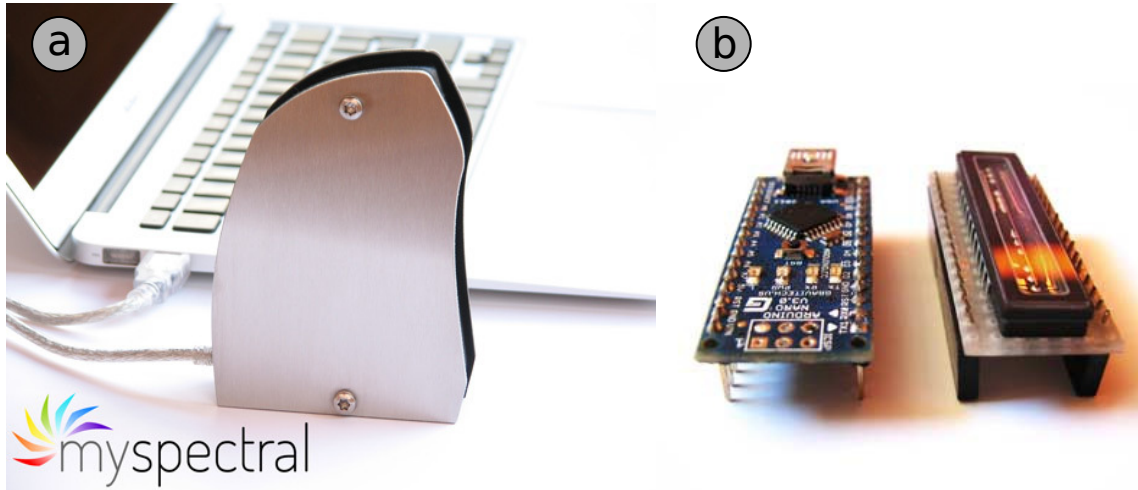


Figure 5.3.: a) The overall design of the Myspectral open-source spectrometer in its aluminum enclosure b) the CCD image sensor (right) is attached on the top of the Arduino Nano board (left). This vertical connection will save space and reduces wire connections. Conversion of analog output signals of the image sensor is carried out in the programmed microcontroller (ATmega328). Images adopted from [112].

final evaluations. The device will automatically distinguish the out-of-range cases and finds the concentration of the Ca based on the in-range sample according to its dilution ratio. A powerful graphical user interface (GUI) is needed to instruct the user towards choosing the right dilution ratio based on the previously stored data.

5.2. Available Technologies

Regarding the available technologies in the scope of spectrometers, assembling the described compact analyzer seems quite feasible. Several internet sources have presented self-made spectrometers, with acceptable optical resolutions. Main elements of these spectrometers are similar to the discussion in Section 2.2: a diffraction grating, a CCD or equivalent image sensor, optical elements such as mirror and lenses and an enclosure to guarantee establishment of proper optical configuration. For instance in reference [112], a fully functional spectrometer, that has an optical resolution as good as 9 nm is introduced. The utilized diffraction grating is a holographic 1300 lines/mm grating, together with a 2000 pixel linear CCD sensor. The analog output signal of the CCD

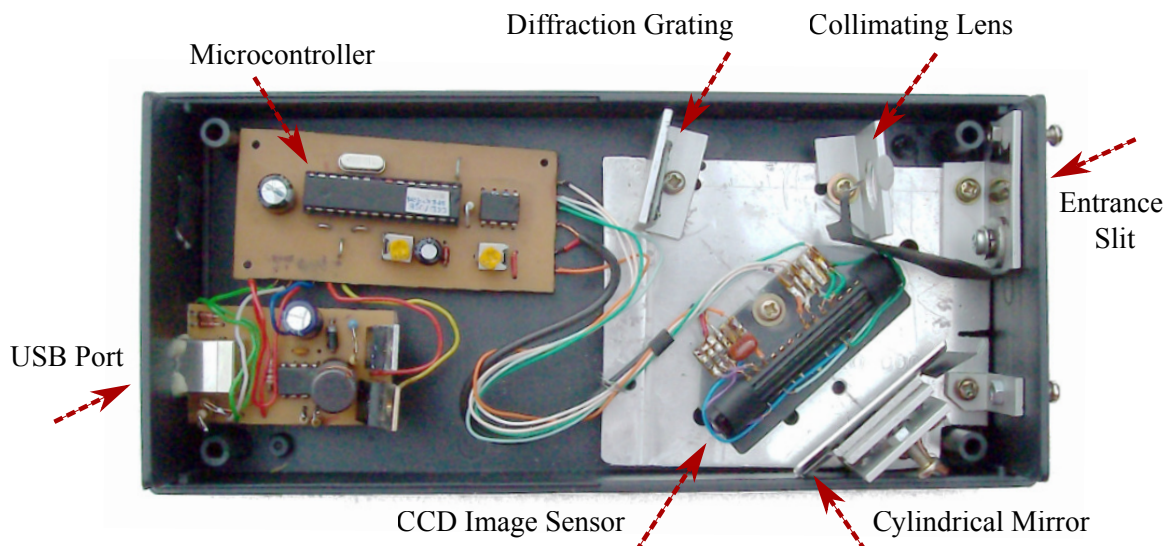


Figure 5.4.: The internal view of the self-made spectrometer from [115]. The diffracted light from the grating is concentrated on the center of the CCD sensor by means of a cylindrical mirror. The image sensor is then connected to the microcontroller and the data will be sent via standard USB port to a computer.

image sensor is digitized and sent to a computer for further analysis. This electronic tasks are handled by a programmable microcontroller ATmega328 (Atmel Corporation, USA), which is commercially available in a prefabricated printed circuit board (PCB) under the trade name Arduino board (Arduino AG, Italy) [113]. The Arduino (Nano version in this case) establishes an interface between the CCD sensor and a computer via universal serial bus (USB). The wavelength range coverage of the device from 380 nm to 750 nm, makes it a good choice for applications in visible light region (Figure 5.3).

Another spectrometer that operates in the range of 400-900 nm, is designed by F.Dominec [114]. In this project, a piece of compact disc serves as diffraction grating and a cylindrical mirror is mounted to focus the diffracted beam to the center of the CCD detector. The CCD output signal is transferred to a computer via USB, after data capturing with ATmega328 microcontroller. The optical resolution between 5 nm and 9 nm was achieved after successful operation of the device. Figure 5.4 illustrates the internal compartments of the spectrometer.

A self-made spectrometer, reported by S.J. Tavener [115], uses the same principles along with a simplified detection circuit. Input light is supplied by an integrated LED. After passing the sample solution, the light beam is collected by a light-dependent

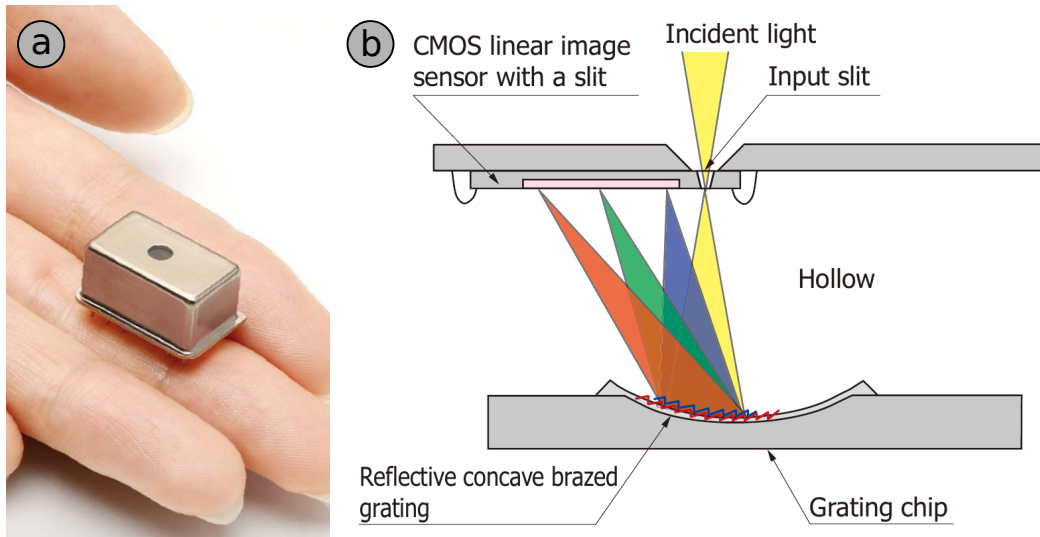


Figure 5.5.: a) Small size of this mini spectrometer by HAMAMATSU can be regarded as a sensor that finds application in several measurement instruments b) light from the input slit reaches the concave grating, diffracted and concentrated at the same time and hits the embedded CMOS linear image. The smart configuration of this sensor, eliminates other optical elements, making all the tasks feasible in a tiny space. Images adopted from [116].

resistor (LDR), amplified by an operational amplifier (Op-Amp) and turned into output current relative to intensity of the incident light.

All these devices provide ideas to build a functional spectrometer. These devices can be further improved and modified in a manner, to be capable of analyzing our microfluidic chips. This can be accomplished by embedding LEDs as the input light source. Change in the color of the RGB LEDs after selecting from the color-wheel, can be managed, for example, via Arduino board for rapid prototyping purposes. A stand-alone device can be fabricated by utilizing a central processing unit (CPU) with more complicated circuitry.

Recent advancements in Micro-Opto-Electro-Mechanical Systems (MOEMS) have led to invention of ultra compact spectrometers, as small as a sugar cube. Light from the input aperture, reaches the reflective concave grating and gets diffracted into the CMOS linear image sensor (Figure 5.5). This spectacular device provides an optical resolution of less than 15 nm (depending on the slit size) in the visible range and can be easily mounted as the main part of a measurement equipment [116].

5.3. Conclusion

In this thesis, we have demonstrated a new determination technique to evaluate the calcium content in human milk. This method is a modification of the routine colorimetric assays, that is combined with microfluidics and hydrogel concept, giving rise to an interdisciplinary approach to a fast analysis technique. The presented method is considered a step forward in measurements and analysis of materials based on their color-change upon reaction with specific indicators. Rapid measurement with low-cost instruments comparing to other analytical methods and consumption of small amounts of sample, are advantages of the stated method, that seem encouraging for further investigations on the topic. Not only for Ca detection, this technique can be generalized to embrace detection of many other materials as well.

A. Human Milk Fortifier

Aptamil FMS



Aptamil FMS

Aptamil
FrauenMilchSupplement

Aptamil FrauenMilchSupplement zur Anreicherung von Frauenmilch für die Ernährung Früh- und Neugeborener mit niedrigem Geburtsgewicht. Mit hoher Energiedichte, hoher Eiweißqualität (extensives Eiweißhydrolysat), Kohlenhydraten, Mineralstoffen, Spurenelementen und Vitaminen.

Aptamil FMS		100 g	4,4 g	100 ml	100 ml Frauen-
Zusammensetzung		Pulver	Pulver	Frauenmilch	Milch + 4,4 g Pulver
Eiweiß	g	25,2	1,1	1,5	2,6
Kohlenhydrate	g	62,2	2,7	7,2	10
Glukose	g	1,1	0,05		0,05
Laktose	g	0,4	0,02	7,2	7,22
Maltose	g	4	0,2		0,2
Polysaccharide	g	51,6	2,3		2,3
Fett	g	0	0	3,5	3,5
Mineralstoffe					
Natrium	mg	803	35	29	64
Kalium	mg	528	23	50	73
Kalzium	mg	1491	66	25	91
Magnesium	mg	115	5	3,1	8,1
Phosphor	mg	872	38	14,2	52,5
Chlorid	mg	573	25	55	80
Eisen	mg	0	0		0
Zink	mg	14	0,61	0,37	0,98
Kupfer	µg	803	35	40	75
Jod	µg	252	11	16,8	27,8
Mangan	µg	183	8,1	0,4	8,5
Energie	kJ	1475	65	280	345
	kcal	347	15	65	80

Aptamil FMS		100 g	4,4 g	100 ml	100 ml Frauen-
Enthält folgende Vitamine:		Pulver	Pulver	Frauenmilch	Milch + 4,4 g Pulver
Vitamin A	µg RE	5275	232	83	315
Vitamin B ₁	mg	3	0,13	0,01	0,14
Vitamin B ₂	mg	4	0,17	0,03	0,2
Vitamin B ₆	mg	2,6	0,11	0,01	0,12
Pantothenensäure	mg	17	0,75	0,2	0,95
Folsäure	µg	688	30	5,1	35,1
Niacin	mg NE	59	2,6	0,2	2,8
Vitamin B ₁₂	µg	4,6	0,2	0,03	0,23
Vitamin C	mg	275	12	4,5	16,5
Vitamin D	µg	115	5	0,2	5,2
Vitamin E	mg	81	3,6	0,24	3,84
Biotin	µg	57	2,5	0,4	2,9
Vitamin K	µg	144	6,4	0,8	7,2
Osmolarität (mos/mol/l)			84	259	380

Indikation: Aptamil FMS ist ein Zusatz, zur Anreicherung von Frauenmilch, für die optimale Ernährung von Früh- und Neugeborenen mit niedrigem Geburtsgewicht. Durch den Zusatz von Aptamil FMS wird die natürliche Zusammensetzung von Frauenmilch dem besonderen Nährstoffbedarf von Frühgeborenen angepasst.
Aptamil FMS ist kein vollständiges Lebensmittel, kein Frauenmilchersatz und nicht zur alleinigen Ernährung geeignet.
Aptamil FMS darf nur unter ärztlicher Kontrolle verwendet werden.

Bibliography

- [1] M. S. Kramer and R. Kakuma, “Optimal duration of exclusive breastfeeding,” *The Cochrane Library*, 2012.
- [2] J. Newman, “How breast milk protects newborns,” *Scientific American*, vol. 273, no. 6, pp. 76–79, 1995.
- [3] Z. Buturovic and S. Ignjatovic, “Breastfeeding and adult intelligence,” *The Lancet Global Health*, vol. 3, no. 9, p. e520, 2015.
- [4] C. G. Victora, R. Bahl, A. J. Barros, G. V. França, S. Horton, J. Krasevec, S. Murch, M. J. Sankar, N. Walker, N. C. Rollins *et al.*, “Breastfeeding in the 21st century: epidemiology, mechanisms, and lifelong effect,” *The Lancet*, vol. 387, no. 10017, pp. 475–490, 2016.
- [5] B. L. Horta and C. G. Victora, “Long-term effects of breastfeeding-a systematic review,” 2013.
- [6] L. M. Gartner, J. Morton, R. A. Lawrence, A. J. Naylor, D. O’Hare, R. J. Schanler, and A. I. Eidelman, “Breastfeeding and the use of human milk,” *Pediatrics*, vol. 115, no. 2, pp. 496–506, 2005.
- [7] M. A. Quigley, G. Henderson, M. Y. Anthony, W. McGuire *et al.*, “Formula milk versus donor breast milk for feeding preterm or low birth weight infants,” *Cochrane Database Syst Rev*, vol. 4, no. 4, 2007.
- [8] D. H. Adamkin and P. G. Radmacher, “Donor human milk: No longer a place for formula in the neonatal intensive care unit?” *Current Pediatrics Reports*, vol. 2, no. 4, pp. 276–283, 2014.
- [9] J. Kulski and P. Hartmann, “Changes in human milk composition during the initiation of lactation,” *Aust J Exp Biol Med Sci*, vol. 59, no. 1, pp. 101–114, 1981.

-
- [10] B. Lönnerdal, "Effects of maternal dietary intake on human milk composition." *The Journal of nutrition*, vol. 116, no. 4, pp. 499–513, 1986.
- [11] D. M. Anderson, F. Williams, R. Merkatz, P. Schulman, D. Kerr, and W. Pittard, "Length of gestation and nutritional composition of human milk." *The American journal of clinical nutrition*, vol. 37, no. 5, pp. 810–814, 1983.
- [12] K. F. Michaelsen, L. Skafté, J. H. Badsberg, and M. Jørgensen, "Variation in macronutrients in human bank milk: influencing factors and implications for human milk banking." *Journal of pediatric gastroenterology and nutrition*, vol. 11, no. 2, pp. 229–239, 1990.
- [13] L. Rosenfeld, *Four centuries of clinical chemistry*. CRC press, 1999.
- [14] A. Balasse. Spectrocolorimetre type d'arsonval ph. & f. pellin. [Online]. Available: http://www.lecompendium.com/dossier_optique_60_colorimetre_pellin/Colorimetre_pellin.htm
- [15] F. D. Snell, *Colorimetric analysis*. D. Van Nostrand Company, 1921.
- [16] N. Colthup, *Introduction to infrared and Raman spectroscopy*. Elsevier, 2012.
- [17] T. Soderberg, "Organic chemistry with a biological emphasis," 2016.
- [18] F. M. Mirabella, *Modern techniques in applied molecular spectroscopy*. John Wiley & Sons, 1998, vol. 14.
- [19] E. B. Wilson, J. C. Decius, and P. C. Cross, *Molecular vibrations: the theory of infrared and Raman vibrational spectra*. Courier Corporation, 2012.
- [20] D. W. Rankin, N. Mitzel, and C. Morrison, *Structural methods in molecular inorganic chemistry*. John Wiley & Sons, 2013.
- [21] D. Sathyanarayana, *Electronic absorption spectroscopy and related techniques*. Universities Press, 2001.
- [22] W. Reusch. Visible and ultraviolet spectroscopy. [Online]. Available: <https://www2.chemistry.msu.edu/faculty/reusch/virttxtjml/spectrpy/uv-vis/spectrum.htm>

-
- [23] A. Gaigalas, L. Wang, H.-J. He, and P. DeRose, “Procedures for wavelength calibration and spectral response correction of ccd array spectrometers,” *Journal of Research of the National Institute of Standards and Technology*, vol. 114, no. 4, p. 1, 2009.
- [24] *Wavelength Calibration Sources*, Ocean Optics. [Online]. Available: <http://oceanoptics.com/product-category/wavelength-calibration-sources/>
- [25] *Light Sources*, Ocean Optics. [Online]. Available: <http://oceanoptics.com/product-category/light-sources/>
- [26] M. W. Davidson, *Tungsten-Halogen Incandescent Lamps*. [Online]. Available: <http://zeiss-campus.magnet.fsu.edu/articles/lightsources/tungstenhalogen.html>
- [27] O. Optics, *An In-Depth Study of the DH-mini Light Source*. [Online]. Available: <http://oceanoptics.com/study-of-dh-mini-light-source/>
- [28] J.-L. Domanchin and J. R. Gilchrist, “Size and spectrum,” *Photonics Spectra*, vol. 35, no. 7, pp. 112–119, 2001.
- [29] *Instruction Sheet for the PASCO Prism Spectrophotometer Kit*, PASCO scientific, 1999.
- [30] Shimadzu, *Fundamentals of UV-Vis-NIR Spectroscopy: Monochromators*. [Online]. Available: <http://www.shimadzu.com/an/uv/support/fundamentals/monochromators.html>
- [31] *Optics Selection Guide Catalog*, Thorlabs, Inc., 2008. [Online]. Available: https://www.thorlabs.com/images/Catalog/V19_08_Optics.pdf
- [32] C. A. Palmer and E. G. Loewen, *Diffraction grating handbook*. Newport Corporation Springfield, Ohio, USA, 2005.
- [33] *The Optics of Spectroscopy*, Newport Corporation. [Online]. Available: <https://www.newport.com/t/grating-physics>
- [34] C. Palmer. Diffraction gratings, the crucial dispersive component. [Online]. Available: <http://www.gratinglab.com/Information/Technical-Publications>
- [35] *The Optics of Spectroscopy*, Horiba Scientific. [Online]. Available: <http://www.horiba.com/us/en/scientific/products/optics-tutorial/>

-
- [36] *Technical Notes: THE BLAZE ARROW*, Richardson Gratings. [Online]. Available: www.gratinglab.com/Information/Technical_Notes/TechNote7.aspx
- [37] *Diffraction Gratings*, Thorlabs, Inc. [Online]. Available: https://www.thorlabs.com/navigation.cfm?guide_id=9
- [38] M. Breidne, S. Johansson, L. Nilsson, and H. Åhlén, “Blazed holographic gratings,” *Journal of Modern Optics*, vol. 26, no. 11, pp. 1427–1441, 1979.
- [39] *Maya2000 Pro Optical Bench Options*, Ocean Optics, Inc. [Online]. Available: <http://oce.oceanoptics.com/product-details/maya2000-pro-optical-bench-options/>
- [40] V. Dhillon, “Astronomical techniques: spectrographs,” University Lecture Notes, 2013. [Online]. Available: http://www.vikdhillon.staff.shef.ac.uk/teaching/phy217/instruments/phy217_inst_course.html
- [41] H. Noda, T. Namioka, and M. Seya, “Design of holographic concave gratings for seya-namioka monochromators,” *JOSA*, vol. 64, no. 8, pp. 1043–1048, 1974.
- [42] G. H. Olsen, A. M. Joshi, S. Mason, K. Woodruff, E. Mykietyn, V. S. Ban, M. Lange, J. Hladky, G. Erickson, and G. A. Gasparian, “Room-temperature ingaas detector arrays for 2.5 μm ,” in *33rd Annual Technical Symposium*. International Society for Optics and Photonics, 1990, pp. 276–282.
- [43] G. H. Olsen, A. M. Joshi, V. Ban, K. Woodruff, G. Gasparian, M. J. Lange, G. Erickson, E. Mykietyn, and S. Forrest, “Multiplexed 256 element ingaas detector arrays for 0.8-1.7 μm room-temperature operation,” in *32nd Annual Technical Symposium*. International Society for Optics and Photonics, 1988, pp. 279–287.
- [44] *Optoelectronic Components: Imaging Detectors*, Warsash Scientific, 2012. [Online]. Available: <http://www.warsash.com.au/products/optoelectronics/IMAGING-DETECTORS.php>
- [45] *What Is A CCD?*, Spectral Instruments, Inc, 2017. [Online]. Available: <http://www.specinst.com/articles.html>
- [46] *Spectrometer Knowledge*, B& W Tek, 2017. [Online]. Available: <http://bwtek.com/spectrometer-part-3a-the-detector/>

-
- [47] *How does my choice of spectrometer slit size affect optical resolution?*, Ocean Optics, Inc. [Online]. Available: <http://oce.oceanoptics.com/faq/choice-slit-size-affect-resolution/>
- [48] A. Mehta. Ultraviolet-visible spectroscopy: Derivation of beer-lambert law. [Online]. Available: <http://pharmaxchange.info/press/author/akul/>
- [49] D. Harvey. Analytical chemistry 2.0. [Online]. Available: http://chem.libretexts.org/Textbook_Maps/Analytical_Chemistry_Textbook_Maps
- [50] C. F. Bohren and E. E. Clothiaux, *Fundamentals of atmospheric radiation: an introduction with 400 problems*. John Wiley & Sons, 2006.
- [51] V. M. Nield and D. A. Keen, *Diffuse neutron scattering from crystalline materials*. Oxford University Press, 2001, vol. 14.
- [52] K.-H. Gericke. Beer-lambert law. [Online]. Available: http://www.pci.tu-bs.de/aggericke/PC4e/Kap_I/beerslaw.htm
- [53] P. Lykos, “The beer-lambert law revisited: A development without calculus,” *J. Chem. Educ*, vol. 69, no. 9, p. 730, 1992.
- [54] *Torus Concave Grating Spectrometer - Installation and Operation Manual*, Ocean Optics, Ocean Optics, Inc., 2013.
- [55] J. Gordon and S. Harman, “A graduated cylinder colorimeter: An investigation of path length and the beer-lambert law,” *J. Chem. Educ*, vol. 79, no. 5, p. 611, 2002.
- [56] J. A. Van Loon, *Analytical atomic absorption spectroscopy: selected methods*. Elsevier, 2012.
- [57] J. S. Casas and J. Sordo, *Lead: chemistry, analytical aspects, environmental impact and health effects*. Elsevier, 2011.
- [58] J. Clark. Using uv-visible absorption spectra. [Online]. Available: <http://www.chemguide.co.uk/analysis/uvvisible/analysis.html>
- [59] Y.-j. Wei, K.-a. Li, and S.-y. Tong, “The interaction of bromophenol blue with proteins in acidic solution,” *Talanta*, vol. 43, no. 1, pp. 1–10, 1996.

-
- [60] M. M. Bradford, "A rapid and sensitive method for the quantitation of microgram quantities of protein utilizing the principle of protein-dye binding," *Analytical biochemistry*, vol. 72, no. 1-2, pp. 248–254, 1976.
- [61] E. Rowatt and R. Williams, "The interaction of cations with the dye arsenazo iii," *Biochemical Journal*, vol. 259, no. 1, pp. 295–298, 1989.
- [62] W. Gratzer and G. Beaven, "Use of the metal-ion indicator, arsenazo iii, in the measurement of calcium binding," *Analytical biochemistry*, vol. 81, no. 1, pp. 118–129, 1977.
- [63] Y. Ogawa, H. Harafuji, and N. Kurebayashi, "Comparison of the characteristics of four metallochromic dyes as potential calcium indicators for biological experiments," *Journal of biochemistry*, vol. 87, no. 5, pp. 1293–1303, 1980.
- [64] K. Ogan and E. R. Simons, "The influence of ph on arsenazo iii," *Analytical biochemistry*, vol. 96, no. 1, pp. 70–76, 1979.
- [65] B. R. Morgan, J. D. Artiss, and B. Zak, "Calcium determination in serum with stable alkaline arsenazo iii and triglyceride clearing," *Clinical chemistry*, vol. 39, no. 8, pp. 1608–1612, 1993.
- [66] S. T. Ohnishi, "A method of estimating the amount of calcium bound to the metallochromic indicator arsenazo iii," *Biochimica et Biophysica Acta (BBA)-General Subjects*, vol. 586, no. 2, pp. 217–230, 1979.
- [67] G. M. Whitesides, "The origins and the future of microfluidics," *Nature*, vol. 442, no. 7101, pp. 368–373, 2006.
- [68] G. V. Casquillas. Introduction to lab-on-a-chip. [Online]. Available: <http://www.elveflow.com/microfluidic-tutorials/>
- [69] G. M. Whitesides and A. D. Stroock, "Flexible methods for microfluidics," *Phys. Today*, vol. 54, no. 6, pp. 42–48, 2001.
- [70] E. W. Young and C. A. Simmons, "Macro-and microscale fluid flow systems for endothelial cell biology," *Lab on a Chip*, vol. 10, no. 2, pp. 143–160, 2010.
- [71] A. A. S. Bhagat, E. T. Peterson, and I. Papautsky, "A passive planar micromixer with obstructions for mixing at low reynolds numbers," *Journal of micromechanics and microengineering*, vol. 17, no. 5, p. 1017, 2007.

-
- [72] D. S. Kim, S. W. Lee, T. H. Kwon, and S. S. Lee, "A barrier embedded chaotic micromixer," *Journal of micromechanics and microengineering*, vol. 14, no. 6, p. 798, 2004.
- [73] V. Hessel, H. Löwe, and F. Schönfeld, "Micromixers—a review on passive and active mixing principles," *Chemical Engineering Science*, vol. 60, no. 8, pp. 2479–2501, 2005.
- [74] C.-Y. Lee, C.-L. Chang, Y.-N. Wang, and L.-M. Fu, "Microfluidic mixing: a review," *International journal of molecular sciences*, vol. 12, no. 5, pp. 3263–3287, 2011.
- [75] Z. Yang, S. Matsumoto, H. Goto, M. Matsumoto, and R. Maeda, "Ultrasonic micromixer for microfluidic systems," *Sensors and Actuators A: Physical*, vol. 93, no. 3, pp. 266–272, 2001.
- [76] S. Wang, Z. Jiao, X. Huang, C. Yang, and N.-T. Nguyen, "Acoustically induced bubbles in a microfluidic channel for mixing enhancement," *Microfluidics and nanofluidics*, vol. 6, no. 6, pp. 847–852, 2009.
- [77] M. Oddy, J. Santiago, and J. Mikkelsen, "Electrokinetic instability micromixing," *Analytical Chemistry*, vol. 73, no. 24, pp. 5822–5832, 2001.
- [78] W.-K. Tseng, J.-L. Lin, W.-C. Sung, S.-H. Chen, and G.-B. Lee, "Active micromixers using surface acoustic waves on y-cut 128 linbo3," *Journal of Micromechanics and Microengineering*, vol. 16, no. 3, p. 539, 2006.
- [79] B. Xu, T. N. Wong, N.-T. Nguyen, Z. Che, and J. C. K. Chai, "Thermal mixing of two miscible fluids in a t-shaped microchannel," *Biomicrofluidics*, vol. 4, no. 4, p. 044102, 2010.
- [80] S. W. Lee, D. S. Kim, S. S. Lee, and T. H. Kwon, "A split and recombination micromixer fabricated in a pdms three-dimensional structure," *Journal of micromechanics and microengineering*, vol. 16, no. 5, p. 1067, 2006.
- [81] P. Löb, H. Pennemann, V. Hessel, and Y. Men, "Impact of fluid path geometry and operating parameters on l/l-dispersion in interdigital micromixers," *Chemical engineering science*, vol. 61, no. 9, pp. 2959–2967, 2006.

-
- [82] S. Hardt, K. Drese, V. Hessel, and F. Schönfeld, “Passive micromixers for applications in the microreactor and μ tas fields,” *Microfluidics and Nanofluidics*, vol. 1, no. 2, pp. 108–118, 2005.
- [83] R. Zengerle, M. Leitner, S. Kluge, and A. Richter, “Carbon dioxide priming of micro liquid systems,” in *Micro Electro Mechanical Systems, 1995, MEMS’95, Proceedings. IEEE*. IEEE, 1995, p. 340.
- [84] G. Takei, M. Nonogi, A. Hibara, T. Kitamori, and H.-B. Kim, “Tuning microchannel wettability and fabrication of multiple-step laplace valves,” *Lab on a Chip*, vol. 7, no. 5, pp. 596–602, 2007.
- [85] P. Vulto, “A lab-on-a-chip for automated rna extraction from bacteria,” Ph.D. dissertation, Zugl.: Freiburg (Breisgau), Univ., Diss., 2008, 2008.
- [86] S. Hakenberg, M. Hügler, M. Weidmann, F. Hufert, G. Dame, and G. A. Urban, “A phaseguided passive batch microfluidic mixing chamber for isothermal amplification,” *Lab on a Chip*, vol. 12, no. 21, pp. 4576–4580, 2012.
- [87] P. Vulto, S. Podszun, P. Meyer, C. Hermann, A. Manz, and G. A. Urban, “Phaseguides: a paradigm shift in microfluidic priming and emptying,” *Lab on a Chip*, vol. 11, no. 9, pp. 1596–1602, 2011.
- [88] D. Puchberger-Enengl, C. Krutzler, F. Keplinger, and M. J. Vellekoop, “Single-step design of hydrogel-based microfluidic assays for rapid diagnostics,” *Lab on a Chip*, vol. 14, no. 2, pp. 378–383, 2014.
- [89] E. M. Ahmed, “Hydrogel: Preparation, characterization, and applications: A review,” *Journal of advanced research*, vol. 6, no. 2, pp. 105–121, 2015.
- [90] O. Okay, “General properties of hydrogels,” in *Hydrogel sensors and actuators*. Springer, 2009, pp. 1–14.
- [91] S. K. Gulrez, G. O. Phillips, and S. Al-Assaf, *Hydrogels: methods of preparation, characterisation and applications*. INTECH Open Access Publisher, 2011.
- [92] K. Deligkaris, T. S. Tadele, W. Olthuis, and A. van den Berg, “Hydrogel-based devices for biomedical applications,” *Sensors and Actuators B: Chemical*, vol. 147, no. 2, pp. 765–774, 2010.

-
- [93] G. Gerlach, M. Guenther, J. Sorber, G. Suchaneck, K.-F. Arndt, and A. Richter, "Chemical and ph sensors based on the swelling behavior of hydrogels," *Sensors and Actuators B: Chemical*, vol. 111, pp. 555–561, 2005.
- [94] R. Bashir, J. Hilt, O. Elibol, A. Gupta, and N. Peppas, "Micromechanical cantilever as an ultrasensitive ph microsensor," *Applied Physics Letters*, vol. 81, no. 16, pp. 3091–3093, 2002.
- [95] D. J. Beebe, J. S. Moore, J. M. Bauer, Q. Yu, R. H. Liu, C. Devadoss, and B.-H. Jo, "Functional hydrogel structures for autonomous flow control inside microfluidic channels," *Nature*, vol. 404, no. 6778, pp. 588–590, Apr 2000. [Online]. Available: <http://dx.doi.org/10.1038/35007047>
- [96] M. Lei, Y. Gu, A. Baldi, R. A. Siegel, and B. Ziaie, "High-resolution technique for fabricating environmentally sensitive hydrogel microstructures," *Langmuir*, vol. 20, no. 21, pp. 8947–8951, 2004.
- [97] D. F. Stamatialis, B. J. Papenburg, M. Gironés, S. Saiful, S. N. Bettahalli, S. Schmitmeier, and M. Wessling, "Medical applications of membranes: drug delivery, artificial organs and tissue engineering," *Journal of Membrane Science*, vol. 308, no. 1, pp. 1–34, 2008.
- [98] C.-B. Laurell, "Quantitative estimation of proteins by electrophoresis in agarose gel containing antibodies," *Analytical biochemistry*, vol. 15, no. 1, pp. 45–52, 1966.
- [99] D. Puchberger-Enengl, S. van den Driesche, C. Krutzler, F. Keplinger, and M. J. Vellekoop, "Hydrogel-based microfluidic incubator for microorganism cultivation and analyses," *Biomicrofluidics*, vol. 9, no. 1, p. 014127, 2015.
- [100] C. Roth, "Agarose low melt instruction," 2014, agaroses for all applications. [Online]. Available: https://www.carlroth.com/downloads/ba/en/6/BA_6351_EN.pdf
- [101] O. Optics. Fiber technical information. [Online]. Available: <http://oceanoptics.com/product-category/fiber-technical-information/>
- [102] G. Fusch, N. Rochow, A. Choi, S. Fusch, S. Poeschl, A. O. Ubah, S.-Y. Lee, P. Raja, and C. Fusch, "Rapid measurement of macronutrients in breast milk: How reliable are infrared milk analyzers?" *Clinical Nutrition*, vol. 34, no. 3, pp. 465–476, 2015.

-
- [103] A. Haller, S. Zauner, A. Managhebaty, D. Puchberger, N. Haiden, A. Kreissl, A. Kasper-Giebl, F. Keplinger, and M. Vellekoop, “Measuring calcium content of human milk on a microfluidic chip,” *Procedia Engineering*, vol. 168, pp. 105–108, 2016.
- [104] Y. Luo, B. Zhang, M. Chen, J. Wang, X. Zhang, W.-y. Gao, J.-f. Huang, and W.-l. Fu, “Rapid and simultaneous determination of essential minerals and trace elements in human milk by improved flame atomic absorption spectroscopy (faas) with microwave digestion,” *Journal of agricultural and food chemistry*, vol. 58, no. 17, pp. 9396–9400, 2010.
- [105] I. J. Griffin, *Perinatal Growth and Nutrition*. CRC Press, 2014.
- [106] R. G. Jensen, B. Blanc, and S. Patton, *Particulate constituents in human and bovine milks*. Academic Press: San Diego, CA, USA, 1995.
- [107] G. Zvaigzne, D. Brogan, and L. Bernstein, “Statistical analysis of the stability of the standard curve for some syva emit assays,” *Clinical chemistry*, vol. 32, no. 3, pp. 437–440, 1986.
- [108] A. Waki, T. Mori, K. Nishijima, K. Honjyo, Y. Kayano, R. Yano, H. Shiraishi, A. Takaoka, Y. Kiyono, and Y. Fujibayashi, “Assessment of validity of the archived standard curve in endotoxin assay,” *Kaku igaku. The Japanese journal of nuclear medicine*, vol. 50, no. 4, pp. 289–296, 2013.
- [109] F. Viénot, H. Brettel, T.-V. Dang, and J. Le Rohellec, “Domain of metamers exciting intrinsically photosensitive retinal ganglion cells (iprgcs) and rods,” *JOSA A*, vol. 29, no. 2, pp. A366–A376, 2012.
- [110] M. Beckler, *Fun with an RGB LED*. [Online]. Available: https://www.mbeckler.org/microcontrollers/rgb_led/
- [111] S. Electronics, *RGB and SMD Light Emitting Diodes*. [Online]. Available: <https://www.sparkfun.com>
- [112] A. Mosat, *Opensource Arduino DIY Spectrometer*. [Online]. Available: <http://myspectral.com/>
- [113] A. AG, *Arduino open-source electronics platform*. [Online]. Available: <https://www.arduino.cc/>

- [114] F. Dominec, “Design and construction of a digital ccd spectrometer,” *Czech Technical University in Prague, Faculty of Nuclear Sciences and Physical Engineering, Department of Physical Electronic*, 2010.
- [115] S. J. Tavener and J. E. Thomas-Oates, “Build your own spectrophotometer,” *EducaTiOn in chEmiSTry*, vol. 44, no. 5, pp. 151–154, 2007.
- [116] H. P. K.K., *Mini Spectrometers*. [Online]. Available: http://www.hamamatsu.com/resources/pdf/ssd/mini-spectro_kacc0002e.pdf